DOE/ET-53088-348 IFSR #348

Computer Simulation of Alfvén Wave Heating

J.L. Geary, J.-N. Leboeuf, and *T. Tajima*
Institute for Fusion Studies
The University of Texas at Austin
Austin, Texas 78712

October 1988

Computer Simulation of Alfvén Wave Heating

J. L. Geary[a], *J.-N. Leboeuf*[b], *and T. Tajima*

Institute for Fusion Studies, University of Texas at Austin, Austin, Texas 78712

ABSTRACT

A particle simulation study of shear Alfvén wave resonance heating is presented. A particle simulation model has been developed for this application that incorporates Darwin's formulation of the electromagnetic fields with a guiding center approximation for electron motion perpendicular to the ambient magnetic field. With this model, we examine several cases of Alfvén wave heating in both uniform and nonuniform simulation systems in a two-dimensional slab. When the antenna parameters match the shear Alfvén resonance condition, the simulation plasmas in the homogeneous cases react strongly with the driven wave. For the inhomogeneous case studies, the kinetic Alfvén wave develops in the vicinity of the shear Alfvén resonance region. The electrons kinetically react with the wave through a collisionless process. The electron velocity distribution function flattens about the parallel phase velocity of the wave with accompanying changes in the spatial structure of the wave. The electron heating rate is in good agreement with the Landau damping model. A substantial electron current is also generated parallel to the applied magnetic field. The ions gain energy by oscillating in the wave electric fields.

---

[a] *present address: Berkeley Research Associates, Springfield, Virginia 22150*

[b] *present address: Oak Ridge National Laboratory, Oak Ridge, Tennesee 37831*

I. INTRODUCTION

The resonant interaction of driven Alfvén waves with a magnetized plasma is studied using particle simulation. Plasma heating using the shear Alfvén resonance was independently proposed by Tataronis and Grossman[1] and by Hasegawa and Chen[2] . This has applies to electron heating in magnetic confinement fusion devices. It is also of importance to space plasmas. This process might be responsible for heating particles in the plasma sheet layer of a magnetospheric substorm[3], for particle acceleration in the aurora[4], and for plasma heating in coronal loops[5]. The Alfvén wave heating scheme was originally conceived as a method where a radio frequency wave, launched at the edge of the plasma, propagates from the edge until it couples its energy to plasma particles in the vicinity of the shear Alfvén resonance layer. In a nonuniform plasma, there exists a singularity in the ideal magnetohydrodynamic (MHD) equations associated with the shear Alfvén resonance in the continuum, ($\omega = k_{||}V_A$). At the singular layer, the wave can propagate only along the magnetic field lines and the wave energy accumulates at the resonance layer, which must eventually be dissipated. This heating scheme has been examined extensively both theoretically[6-11] and experimentally[12-17] for more than a decade. However some important features are still not well understood. Difficulties lie in the complicated geometries of the laboratory experiments, strong influence of surface effects, and nonlinear effects. A full kinetic treatment of Alfvén waves in a magnetized nonuniform plasma is a formidable theoretical problem to investigate analytically.

Through this investigation, we present an attempt to apply a fully nonlinear, electromagnetic particle simulation code[18] to Alfvén wave resonance heating and to confirmation of the Alfvén wave mode conversion. Particle simulation codes follow the temporal evolution of the problem while self-consistently including kinetic effects and nonlinearities. Particle simulation of kinetic Alfvén wave heating has also been performed by Tanaka

et al.[19]. In their simulations a monochromatic plane wave is initially established in the plasma while the wave is launched by an antenna in our case. Their simulations examined doubly-periodic systems whereas our simulations include bounded, nonuniform systems. Other theoretical investigations have mostly examined the linear, stationary response of the plasma to an antenna. However, some of the experimental results are not easily understood from such linear, stationary analyses. A primary goal of this work is to pinpoint important areas that may not have received sufficient attention thus far. Since it is difficult to represent all the aspects of a confinement device in a computer model, it becomes necessary to idealize the geometry and reduce the temporal and spatial scales to times and lengths manageable in a computer model.

The standard particle simulation codes available to us either were too computationally expensive or did not incorporate enough physics in the model. For this purpose, a new computer model was developed that incorporates a massless guiding center model for electron motion perpendicular to the magnetic field with Darwin's radiationless (magnetoinductive) model for the full electric and magnetic fields. This simulation model is discussed in Section II. The reaction of the simulation plasma to an external source of RF energy, whose frequency is in the Alfvén wave frequency range, is presented in a number of case studies in Section III. The details of the wave dynamics, heating processes, and the effects the wave has on the plasma properties are examined when the plasma is homogeneous and when an inhomogeneity is introduced by varying the magnetic field. Finally, Section IV summarizes the paper.

II. COMPUTATIONAL MODEL

The computational model that we found suitable for this application combined Darwin's magnetoinductive model for the electric and magnetic fields with a guiding center scheme for electron motion perpendicular to the magnetic field which is described in more

detail by Geary et. al.[18]. The magnetoinductive approximation eliminates light wave propagation. The magnetoinductive model is nonradiative in character and thus has a lower overall background noise level than fully electromagnetic codes while retaining self-consistent electric and magnetic fields. Both radiation and the full details of the electron gyromotion are assumed not to be necessary for the description of Alfvén waves or of the important dissipation processes. A simpler version, which neglects compressional Alfvén waves, has been used by Lee et. al.[20] to investigate anomalous transport due to shear Alfvén waves.

Electron motion perpendicular to the magnetic field follows the $\mathbf{E} \times \mathbf{B}$ motion of the guiding center while the electron motion parallel to the magnetic field retains full dynamics. Thus parallel kinetic effects resulting from finite electron inertia are retained. The resulting equations of motion for electrons are

$$\begin{aligned} \frac{d\mathbf{v}_{e\|}}{dt} &= -\frac{e}{m}\mathbf{E}_{\|} \\ \mathbf{v}_{e\perp} &= \frac{c}{B_0^2}\mathbf{E} \times \mathbf{B}_0 \\ \frac{d\mathbf{x}_e}{dt} &= \mathbf{v}_e, \end{aligned} \tag{1}$$

where $\mathbf{E}_{\|}(\mathbf{x}) = \hat{b}(\mathbf{x})\left[\hat{b}(\mathbf{x}) \cdot \mathbf{E}(\mathbf{x})\right]$ and where $\hat{b}(\mathbf{x}) = \mathbf{B}_0(\mathbf{x})/B_0(\mathbf{x})$. The time step used to advance the simulation can greatly exceed the electron gyrotron period. The ion motion in this code model is governed by the full nonrelativistic Newton-Lorentz equations of motion

$$\begin{aligned} \frac{d\mathbf{v}_i}{dt} &= \frac{e}{M}\mathbf{E} + \frac{e}{Mc}\mathbf{v}_i \times \mathbf{B} \\ \frac{d\mathbf{x}_i}{dt} &= \mathbf{v}_i \end{aligned} \tag{2}$$

This model contains the essential ingredients of particle motion for simulation of Alfvén wave heating processes. The $\mathbf{E} \times \mathbf{B}$ motion of the electrons is necessary for the existence of Alfvén waves. Electron Landau damping, which is expected to be a primary heating

mechanism, is included in our model. The Alfvén wave frequency and the ion gyrofrequency are too close to treat ions as guiding center particles. Moreover, finite ion Larmor radius effects are essential to the nature of the kinetic Alfvén wave. The particle equations of motion are advanced in time by the combination of a predictor-corrector scheme for the perpendicular electron motion and a leapfrog scheme for the ion motion and parallel electron motion.

The magnetoinductive field equations are

$$\nabla \times \mathbf{E}_T = -\frac{1}{c}\frac{\partial \mathbf{B}}{\partial t} \tag{3}$$

$$\nabla \times \mathbf{B} = \frac{4\pi}{c}\mathbf{J}_T \tag{4}$$

$$\nabla \cdot \mathbf{E}_L = 4\pi\rho \tag{5}$$

$$\nabla \cdot \mathbf{B} = 0 \tag{6}$$

where the subscript T denotes the divergence-free (transverse) and where the subscript L denotes the curl-free (longitudinal) components of a vector. With these definitions, $\mathbf{E}_L$ and $\mathbf{E}_T$ satisfy

$$\nabla \times \mathbf{E}_L = \nabla \cdot \mathbf{E}_T = 0.$$

The words longitudinal and transverse will refer to the curl-free and divergence-free components of a vector. A key feature of the magnetionductive model is that information is transmitted instantaneously. Magnetic induction from Faraday's law, Eq. (3), is still retained.

The particle simulation code employed here has $2\frac{1}{2}$ dimensions, i.e., two spatial coordinates (x, y) and three velocity components (v_x, v_y, v_z). The z-direction is ignorable. The finite size particles, or quasiparticles, are Gaussian-shaped. The background magnetic field vector lies in the $y - z$ plane. An external source in the shape of a sheet antenna is located at approximately the centerline of the x-direction. The antenna current flows

in the z-direction preserving the charge neutrality of the antenna. A sinusoidal travelling wave is launched by an antenna current of the form

$$\mathbf{J}_A(\mathbf{x}) = J_A S(x - x_A) sin(\omega_A t - k_A y)\hat{z} \tag{7}$$

where J_A, ω_A, and k_A are the amplitude, frequency, and wavenumber of the antenna and where x_A is the x-coordinate of the antenna current sheet. Because of the periodicity of the y-direction, the antenna wavenumber k_A is restricted to be an integer multiple of the fundamental wavenumber of the grid in the y-direction. Finite size particle effects act to broaden the current sheet such that it effectively has a small but finite spatial extent in the x-direction.

The strength of the antenna is normalized in terms of a parameter W, the energy of the source integrated over the simulation volume divided by the initial thermal energy of all the particles in the simulation,

$$W = \int_V \frac{B_A^2 + E_A^2}{8\pi} d\mathbf{x} \Big/ \sum_j^{\substack{all \\ particles}} \frac{1}{2} m_{pj} v_j^2. \tag{8}$$

The antenna fields $\mathbf{B}_A$ and $\mathbf{E}_A$ are calculated including the presence of the plasma assuming that the particles in the plasma have an effectively zero temperature. The ambient magnetic field direction is constrained to lie in the $y - z$ plane. With θ defined by $\theta = \tan^{-1}(B_y/B_z)$, the parallel wavenumber is given by $k_{||} = k_y \sin\theta$. Thus the antenna launches a single coherent mode propagating obliquely to the magnetic field. For the results presented in this paper,the condition $B_{0z} \gg B_{0y}$ will apply (small θ). The finite particle size is held fixed at $a_x \times a_y = 1.5\Delta \times 15\Delta$. The simulations begin with with initially equal ion and electron temperatures, $T_i = T_e$. To clearly separate the Alfvén wave resonance effects from ion cyclotron resonance effects, it is desirable to place the kinetic Alfvén wave resonance frequency well below the ion gyrofrequency. This places strict demands on the range of parameters in the present computer model.

Simulation results are presented from codes that are either bounded or periodic in the x-direction and that are periodic in the y-direction. The bounding technique assumes the existence of mirror systems adjacent to the active simulation region. The image particles carry the same charge and execute the same motion as the corresponding particles in the active system. Particles crossing a periodic boundary are reinserted at the opposite edge. Particles crossing an image boundary are reflected using Method I of Natiou et al.[21].

III. SIMULATION RESULTS

The behavior of a simulation plasma is examined in a number of computer experiments. Our aim is to point out important effects and explain the results in terms of simple physical concepts. The computer results may be important in a sense that they indicate those areas that may require closer examination in future theoretical and experimental work. The first set of simulations discusses the behavior of a simple system, a homogeneous plasma with periodic boundaries. The plasma responses to resonant and nonresonant excitations are analyzed. In the final set, the plasma behavior is investigated when a nouniform magnetic field introduces inhomogeneity to the bounded system.

A. Elementary Theoretical Considerations

Tataronis and Grossman[1] and Hasegawa and Chen[2] pointed out by that the Shear Alfven wave singularity in the MHD equations could be utilized to heat the plasma. Let us consider a slab model that is nonuniform in the x-direction and assume solutions to the MHD equations of the form

$$\mathbf{v} = \mathbf{v}(x)e^{-i\omega t}e^{i(k_y y + k_z z)}$$

where $\mathbf{B}_0$ lies in the z-direction. Using ideal MHD, the wave equation can be written[2]

$$\frac{d}{dx}\left[\frac{\varepsilon\alpha B^2}{\alpha B^2 k_\perp(x) - \varepsilon}\frac{dv_x}{dx}\right] - \varepsilon v_x = 0 \tag{9}$$

where

$$\varepsilon(x) = \omega^2 4\pi\rho(x) - k_{||}^2(x)B^2(x),$$

and where

$$\alpha(x) = 1 + \frac{\omega^2 c_s^2(x)}{v_A^2(x)[\omega^2 - k_{||}^2 c_s^2(x)]}.$$

The singularity in the differential Eq.(9) occurs when $\varepsilon(x) = 0$. An electromagnetic wave with frequency ω will satisfy the resonance condition of a point x_s when $\omega = k_{||}(x_s)v_A(x_s)$. There exists a continuous range of frequencies that satisfy the resonance condition bounded by $(k_{||}v_A)^2_{min} < \omega^2 < (k_{||}v_A)^2_{max}$. If an external source of RF energy can excite a resonant wave at the singular point $x = x_s$, the singular property of the shear Alfvén wave permits the wave to propagate only along the magnetic field lines. Thus the wave energy accumulates at the resonance layer. Because of the existence of a continuous frequency spectrum, the wave energy may be dissipated by "phase mixing" at the resonance layer. The inclusion of kinetic effects[6,7] modifies the properties of the shear Alfvén wave solutions, often termed the kinetic Alfvén wave, from the MHD solutions. When the ions maintain their finite Larmor radius, a charge separation between the electrons and ions develop which generates significant longitudinal (electrostatic) electric fields. These longitudinal electric fields can be much larger than the transverse (inductive) electric fields associated with the kinetic Alfvén wave. For parameters in contemporary laboratory devices, collisionless damping is expected to dominate over collisional heating.

We therefore examine heating by Landau damping. The change in kinetic energy U in a volume V is given by

$$\frac{dU}{dt} = \frac{1}{2} Re\left[\int_V \mathbf{J}_\mathbf{e}^* \cdot \mathbf{E} + \mathbf{J}_\mathbf{i}^* \cdot \mathbf{E} dx\right]. \tag{10}$$

The first term on the right side of Eq.(10) is the electron absorption and the second term is the ion absorption. Assuming a Maxwellian electron distribution function, the change

in electron energy is given by

$$\frac{dU_e}{dt} = \delta_e \frac{\omega_{pe}^2}{\omega} \int_V \frac{|E_\parallel|^2}{8\pi} dx \tag{11}$$

where

$$\delta_e = \sqrt{\frac{\pi}{2}} z^3 e^{-z^2/2}$$

and where

$$z = \frac{\omega}{k_\parallel} \sqrt{\frac{m}{T_e}} = \frac{\omega}{k_\parallel V_{Te}}.$$

The heating rate from Eq.(11) achieves its maximum value when $z = 1$. In the resonance region where $\omega = k_\parallel V_A$, this is equivalent to $V_{Te} = \omega/k_\parallel = V_A$. A calculation for the ion Landau damping rate[6] contains a similar exponential dependence with a term $\exp[-V_A^2/2V_{Ti}^2]$. The ion heating by Landau damping is therefore negligibly small for a low-β plasma. If the plasma β is smaller than 0.1, electron Landau damping is expected to dominate collisionless absorption processes.

In an experimental device, such as a tokamak, an antenna located at the plasma edge launches an electromagnetic wave. The shear component of this wave is strongly damped at the edge. It is expected that the coupling to the Alfvén wave resonance region occurs through the weakly evanescent compressional component. The antenna configuration should be approximately the same shape as the resonance mode for maximum coupling. It has been pointed out by Stix [24] that for the wave to propagate across the density gradient from the antenna to the resonance region, either $\beta_e > \sqrt{m_e/M_i}$ or $\beta_i > \sqrt{m_e/M_i}$. If neither condition is satisfied, the kinetic Alfvén wave is better described by cold plasma equations and is reflected from the resonance region forming a surface mode. This result has been confirmed by the numerical studies of Ross et al.[7].

B. Driven Alfvén Waves in a Periodic, Uniform Plasma

We start with a homogeneous magnetized plasma slab in an unbounded system. The plasma behavior is investigated for one example when the wave generated by the antenna does not resonate with the plasma and for three examples when the antenna driven wave satisfies the Alfvén wave resonance conditions. The nonresonant case displays weak coupling between the plasma and the antenna, while the resonant cases show strong coupling between them.

1. Nonresonant

The first example does not match the frequency and wavenumber of the antenna current with any plasma resonance. For this nonresonant run, the plasma β is low, $\beta = 2.7 \times 10^{-4}$. An ion-to-electron mass ratio of $M/m = 1600$ is used with a time step of $\omega_{pe}\Delta t = 15.0$. The angle θ has the value $\theta = 3.1°$. The oscillator frequency, $\omega_A = 2.9 \times 10^{-3}\omega_{pe}$, is below the ion cyclotron frequency, $\Omega_i = 8.3 \times 10^{-3}\omega_{pe}$, such that ion cyclotron resonance effects are not expected. The electron thermal velocity has the value $V_{Te} = 0.4\omega_{pe}\Delta$ and the Alfvén velocity has the value $V_A = 1.0\omega_{pe}\Delta$. The ion Larmor radius is a little larger than the grid spacing, $\rho_i = 1.2\Delta$. The antenna wavenumber is given the fundamental value of the system, $k_A\Delta = 2\pi\Delta/L_y = 1.96 \times 10^{-2}$ and the antenna strength is $W = 8.6 \times 10^{-3}$. The parallel phase velocity of the wave is $(V_{ph})_{||} \equiv \omega_A/(k_A sin\theta) = 2.79\omega_{pe}\Delta$ which is significantly larger than the Alfvén speed. There are four particles of each species per grid cell. The simulation size is $L_x \times L_y = 64\Delta \times 320\Delta$. The plasma parameters chosen for this run are closest to the values near the edge of present toroidal experiments.

The dominant wave patterns driven by the antenna are characterized by the antenna wavenumber in the y-direction and the grid fundamental wavenumber in the x-direction. For the duration of the run until $\omega_{pe}t = 13000$, the electric and magnetic fields directly driven by the antenna maintain a standing wave pattern in the x-direction while propa-

gating forward in the y-direction. The time evolution of the total electromagnetic field energy and the ion and electron kinetic energies portrayed in Fig. 1 indicate that the wave driven by the antenna couples weakly to the plasma. The electromagnetic field energy and the total ion kinetic energy do not show an appreciable time averaged increase in value. However, both of these energies oscillate out of phase with each other suggesting that there is an energy exchange occurring between the ions and the electromagnetic fields. These oscillations have a frequency that is approximately twice the shear Alfvén resonance frequency for the antenna wavenumber. The electrons do not appear to participate in this energy exchange. The electrons have an average gain in kinetic energy of 2.5% which is a small value compared to the resonant cases.

2. Resonant: V_A=V_{te}

For the first resonant case, the parallel phase velocity of the wave is equal to the electron thermal velocity. It is expected that this parameter range will maximize the collisionless electron heating. The plasma β for this case is fairly low with $\beta = 1.7 \times 10^{-3}$. The plasma parameters that are different from the nonresonant case are $V_{Te} = 1.0\omega_{pe}\Delta$ and $\rho_i = 3.0\Delta$. The antenna parameters have the values: $\omega_A = 1.08 \times 10^{-3}\omega_{pe}, k_A\Delta = 1.96 \times 10^{-2}$, and $W = 3.1 \times 10^{-3}$. The parallel phase velocity of the antenna driven wave is therefore $(V_{ph})_{||} = 1.0\omega_{pe}\Delta$ which matches the Alfven velocity and the electron thermal speed. The excitation frequency is almost a factor of 8 below the ion cyclotron frequency. The simulation ran to time $\omega_{pe}t = 36000$ which is approximately 6.2 periods of the antenna wave. At a later time $\omega_{pe}t = 24000$, the kinetic Alfvén wave strongly establishes itself from the initial input wave, as can be seen in Figs. 2 and 3. The excited wave forms a standing wave structure in the x-direction and propagate with the antenna current in the y-direction. Particulary indicative of the kinetic Alfvén wave are the mode structures seen in Fig. 3 of the longitudinal electric fields, which are entirely due to the plasma response.

The magnetic fields B_x and B_y are derivable from a single vector potential component A_z (since $\partial/\partial z = 0$) and the electrostatic fields are derivable from an electrostatic potential Φ. The wave propagating in Figs. 2 and 3 has the feature that the electrostatic potential Φ has the same phase as the vector potential A_z. This wave has properties consistent with what is expected of the kinetic Alfvén wave. These wave patterns are established for all three resonant examples in this section.

The wave significantly modifies the electron velocity distribution function parallel to the magnetic field as shown in Fig. 4. The velocity distribution function is flattened at the parallel phase velocity of the wave. The effect is so strong in this case, that in contrast to the initial Maxwellian shape peaked about $V_e = 0$, the distribution function at later times does not exhibit a substantial peak in the range $-0.5 < V_e/(V_{Te}) < 1.5$. As expected, significant electron heating is observed which is spatially peaked near the antenna position with a secondary peak occurring approximately one-half of the system's length away. The peaks occur where the electric fields with parallel components, E_{Ly} and E_{Tz}, are at their maximum strength. This information supports the conclusion that Landau damping is the mechanism heating electrons. The maximum of the spatially localized electron temperature is 250% above its initial value at $\omega_{pe}t = 36000$.

There is also a substantial increase in the measured ion temperature in all three resonant examples. Separate ion temperatures are associated with different ion velocity components. For example, the ion x-temperature T_{ix} is defined as

$$\frac{1}{2}T_{ix} = \frac{1}{2}M\sum_{j}^{ions}(V_{jx}^2 - \langle V_x\rangle^2)$$

and where

$$\langle V_x\rangle = \sum_{j}^{ions} V_{jx}.$$

similar definitions apply to the temperatures T_{iy}, T_{iz}, $T_{i\perp}$ and $T_{i\|}$. The spatial profiles of the ion y-temperature T_{iy} exhibit two peaks of roughly equal magnitude positioned on both

sides of the antenna. These peaks are located approximately where the electron heating is at a minimum. The spatial profiles of the ion temperatures T_{ix} and T_{iz} do not display noticeable changes from their initial shapes. The ion temperature increase is adequately explained as ion oscillation motion produced by the electric fields of the kinetic Alfvén wave. The wave electric fields couple to the ions via $\mathbf{E} \times \mathbf{B}$ motion. This agrees with the observation that the maxima of T_{iy} coincide with the biggest contour values of E_{Lx}, which is the largest of the wave electric fields. The temperature increase does not represent a true increase in the thermalization of the ion motion. To get a true thermalization, some mechanism, such as collisionality, would have to interrupt the regularity of the motion effectively mixing the phase of the ion oscillation with respect to the wave oscillation.

The time evolution of the electromagnetic field energy depicted in Fig. 5 is enhanced over its initial values. The field energy grows by over a factor of seventy above the initial wave energy during the first five periods before reaching a saturation level. The saturation is reached when the electron distribution function is flattened about the phase velocity of the wave thereby quenching the absorption from Landau damping. Energy is exchanged between the ions and the excited wave at twice the antenna frequency. In dimensionless units, the total field energy increases by 0.22 while the ions increase 0.15 indicating there is roughly an equal division of wave energy between the ions and the electromagnetic fields. The electron kinetic energy keeps increasing over the full length of the run. The electron energy increases 112% above the initial thermal value. The greatest share of the ion energy increase is seen in the ion temperature $T_{i\perp}$ and the remainder goes to T_{ix}. The ion parallel temperature is not significantly affected by the kinetic Alfvén wave. The collisionless electron damping also generates a substantial electron current. By the end of the run, the electrons gain a net drift velocity which is 39% of the initial thermal velocity.

3. Resonant: $V_A < V_{te}$

The next case examined in this section is characterized by an electron thermal velocity larger than the parallel phase velocity of the wave. This is the largest β case presented in this section with the value $\beta = 9.5 \times 10^{-3}$. These parameters are probably closest to the conditions at the resonant surface for a toroidal device such as the PRETEXT or TCA tokamaks of the cases presented. The other plasma parameters for this run are: $M/m = 900$, $V_{Te} = 1.2\omega_{pe}\Delta, \Omega_i = 7.5 \times 10^{-3}\omega_{pe}, \rho_i = 5.4\Delta, \theta = 6.3°$, and $\omega_{pe}\Delta t = 8.0$. The antenna parameters have the values $\omega_A = 1.44\times10^{-3}\omega_{pe}, k_A\Delta = 1.96\times10^{-2}$ and $W = 8.6\times10^{-3}$. The system is followed to time $\omega_{pe}t = 24000$ which is 5.5 periods of the antenna. The parallel phase velocity of the wave is $(V_{ph})_{||} = 0.67\omega_{pe}\Delta$ or $(V_{ph})_{||}/V_{Te} = 0.56$. The heating efficiency of the electrons from Landau damping is expected to be somewhat less than the last case.

The wave structures of the electric and magnetic fields initially form the patterns of the kinetic Alfvén wave propagating in the y-direction and with a standing wave structure in the x-direction similar to Figs. 2 and 3. At a later time however, $\omega_{pe}t = 19200$, the contours of the wave fields have changed, as seen from Fig. 6. The phase fronts are at an oblique angle with respect to the y-axis rather than perpendicular to it. At this point in the simulation, both the particles and the electromagnetic fields are losing energy. The simulation plasma gives energy back to the antenna rather than absorbing energy. By the end of the run of $\omega_{pe}t = 24000$, the wave structure recovers its previous shape. The electron absorption again appears consistent with expectations from Landau damping. As can be observed from Fig. 7, the electron distribution is smoothed about the parallel phase velocity of the wave at time $\omega_{pe}t = 12000$. By the end of the run, $\omega_{pe}t = 24000$, the peak of the distribution function has shifted towards that value.

The total electromagnetic field energy reaches a saturation level quickly at $\omega_{pe}t = 10400$ after 2.3 wave periods, as seen from Fig. 8. The field energy then undergoes a subsequent decline to a minimum level approximately at $\omega_{pe}t = 19000$ and later is

increasing again by the completion of the run. The maximum gain of the field energy is about 12.5 times the initial antenna value. The ion and electron kinetic energies increase or decrease when the total field energy increases or decreases. The maximum gain of the ion kinetic energy is about 10% above its initial value and the maximum gain of the electron kinetic energy is 31% above its initial value. The electrons are also driven in the direction of wave propagation. The maximum average drift electron speed is about 18% of the initial thermal speed. The wave growth and plasma heating is smaller than the previous case. The plasma saturates at a much lower level and for a time drives energy back into the antenna.

4. Resonant: $V_A > V_{te}$

The parallel phase velocity of the wave is larger than the electron thermal velocity for the third resonant case presented here. The plasma β is low for this example with the value $\beta = 2.3 \times 10^{-4}$. Other plasma parameters have the values: $M/m = 900, V_{Te} = 0.75\omega_{pe}\Delta, \Omega_i = 9.9 \times 10^{-3}\omega_{pe}, \rho_i = 2.5\Delta, V_A = 2.67\omega_{pe}\Delta, \theta = 3.1°$ and $\omega_{pe}\Delta t = 10$. The antenna parameters have the values: $\omega_A = 2.46 \times 10^{-3}\omega_{pe}, k_A\Delta = 1.96 \times 10^{-2}$, and $W = 6.8 \times 10^{-3}$. The antenna frequency is about one-fourth of the ion cyclotron frequency so ion cyclotron resonance effects are not expected. The system is evolved to $\omega_{pe}t = 16000$ which is 6.3 wave periods.

The kinetic Alfvén wave that has been excited accelerates electrons in the parallel direction generating substantial currents in the plasma. These currents in turn significantly modify the wave fields. These currents appear to shift the wave to the left in the x-direction. As is shown in Fig. 9, by the completion of the run, the wave has moved to the left approximately 10Δ which is 16% of the system length. The wave is acting to trap electrons and accelerate them. The trapping creates an energetic tail on the electron velocity distribution function parallel to the magnetic fields, as is shown in Fig.

10. The spatial structure can be inferred from the $x - V_{||}$ phase space scatter plots of the electrons in Fig. 11. The maximum trapping occurs near the antenna but is not symmetric about the antenna. It is stronger to the left of the antenna than to the right, probably explaining the shift of the wave fields. As is expected in trapping phenomena, the maximum velocity achieved by the electrons is double the parallel phase velocity of the wave, which is $2(V_{ph})_{||} = 6.1V_{Te}$. There are large increases in the electron temperature. The heating is strongest near the antenna and is spatially symmetric about the antenna position. There is a secondary maximum in the electron temperature at $L_x/2$ away from the x-coordinate of the antenna. The maximum electron temperature increase is about 640% above initial values.

The electromagnetic field energy reaches a maximum after approximately 3 periods as can be recognized from Fig. 12, eventually declining in magnitude. The maximum increase in field energy is over 5 times above the initial antenna contribution. The total energy gain of the electrons is about 160%. The wave interaction affects the electrons far more intensely than the ions. The trapping and acceleration gives the electrons an average drift velocity which is approximately 30% of the initial electron thermal velocity. A small parallel drift of the ions develops but its value is only 2% of the initial ion thermal velocity. The wave again saturates at a lower level than case 2 where $V_A = V_{Te}$. Since electrons are trapped by the wave, the electron temperature increases greatly and a strong current is driven.

Simulation runs of an unbounded, uniform plasma driven by an external source have been presented from four different parameter regimes. In the first case, the antenna wavenumber and frequency do not match a plasma resonance. The simulation plasma exhibited weak coupling to the driven wave as a consequence. The antenna wavenumber and frequency matched the shear Alfvén resonance values for the three remaining cases. These three examples are primarily distinguished by differing values of the Alfvén speed

with respect to the electron thermal speed. All three resonant cases displayed strong interaction between the antenna driven wave and the plasma with the electromagnetic field energy increasing at least several times above the initial pump amplitude. Substantial electrostatic electric fields characteristic of the kinetic Alfvén wave develop to accompany the inductive fields driven by the antenna. When $V_A \simeq 3V_{Te}$, electron trapping is the dominant process in the system. The electron distribution function develops a large non-thermal tail with a maximum speed equal to twice the parallel phase velocity of the driven wave. The other two resonant cases exhibit smoothing, whose width is the order of the phase velocity, of the electron distribution function about the parallel phase velocity of the wave. The electron heating and currents are produced by collisionless absorption of the wave. An increase in ion temperature is observed but it does not represent a true thermalization of the wave. This increase represents the portion of total wave energy that resides in the ion motion.

C. Driven Alfvén Waves in a Bounded, Nonuniform Plasma

Thus far, the excitation of kinetic Alfvén waves and associated heating processes have been examined in homogeneous plasmas. For the Alfvén wave resonance heating scheme, the variation of plasma parameters plays an essential role. We are particularly interested in the situation in which the plasma contains a shear Alfvén resonance layer. The results in this section are therefore a step closer to experimentally relevant situations. The bounded model is used for the nonuniform cases presented here. Both of the examples considered in this section contain an Alfvén wave resonance layer. There is an example where $V_A = V_{Te}$ is satisfied at the resonance layer and an example where $V_A < V_{Te}$ at the resonance layer. When $V_A > V_{Te}$ at the resonance layer, the wave does not penetrate so this case is not examined here[7].

The variation of the density is an important nonuniformity present in the laboratory

experiments. In our numerical model the algorithm scheme of renormalization used to solve the transverse electric field involves an iteration about the peturbed density. A density gradient is likely to worsen the convergence properties of this iterative field solver. Instead, in the present model, the nonuniformity in the Alfvén velocity is introduced through the variation of the externally imposed magnetic field. This is accomplished in a manner that does not degrade the solution for the transverse electric field. The ambient magnetic field is varied by the relation

$$B_y(x) \propto B_z(x) \propto B_0(x) = \frac{B_0(x = x_{res})}{[a(x - x_{res}) + 1.0]^{1/2}}$$

where the variable a is related to the magnetic field scale length L_{res} at the resonance layer by $a = -2/L_{res}$. The angle θ between the y- and z-components of the ambient magnetic field maintains a constant value throughout the plasma for this type of variation. The center of the resonance layer is chosen to coincide with the center of the active system, i.e., $x_{res} = L_x/2$. For the cases presented in this section, the ions and electrons have initially equal temperatures, $T_i = T_e$. The antenna excites a single mode travelling wave given by Eq. (7). The simulation size is $L_x \times L_y = 64\Delta \times 320\Delta$. The magnetic field scale length is $L_{res} = 100\Delta$. Quantities that depend on the magnetic field will be quoted by their values at the resonance layer.

1. $V_A(x_{res})=V_{te}$

The first nonuniform case we examine has the Alfvén speed at the resonance layer equal to the electron thermal velocity, i.e., $V_A(x_{res}) = V_{Te}$ where it is expected that electron heating will be maximized. The plasma parameters at the resonance layer are the same as the first resonant case 2 in subsection B. The antenna parameters are assigned the values: $\omega_A = 1.08 \times 10^{-3}\omega_{pe}, k_A\Delta = 1.96 \times 10^{-2}$, and $W = 6.5 \times 10^{-3}$. The variation of the Alfvén speed with x is graphically depicted in Fig. 13. The magnetic field has its

maximum value at the boundary where the antenna is placed. This simulation evolved to time $\omega_{pe}t = 54000$ which corresponds to 9.3 wave periods.

The Fourier transformed values of the electric and magnetic fields, $\mathbf{E}_L(\mathrm{k},t), \mathbf{E}_T(\mathrm{k},t)$, and $\mathbf{B}(\mathrm{k},t)$, are stored on disk for subsequent analysis. We display the field energy density spectrum $|E(x,k_y,t)|^2$ where x and t are varied and k_y is held fixed. The energy density spectra for the field components $|E_{Tz}(x,k_A,t)|^2, |B_x(x,k_A,t)|^2$, and $|E_{Ly}(x,k_A,t)|^2$ are shown in Fig. 14 from different perspectives. The E_{Ly} spectrum is not directly generated by the antenna but is due only to the plasma response. For the plots in Fig. 14, the lines running parallel to the time axis show the temporal variation at a particular spatial position with each line representing an average over three grid points. The lines running parallel to the x-axis similarly show the spatial variation at a given time interval with each line representing an average over one-fourth of an antenna period.

Inspection of Fig. 14 demonstrates the development of an Alfvén wave near the resonance indicating that mode conversion has occurred. However the wave is stronger in the region adjacent to the antenna. The mode converted kinetic Alfvén wave grows during the initial 1.5 wave periods of the simulation. The amplitude of the wave energy in the resonance region is fairly constant for the following two periods. A decline in amplitude then occurs after $\omega_{pe}t = 20000$. The peak of the mode converted wave is shifted towards smaller x than what is expected. The boundaries may influence the location of the mode conversion region since the system length in the x-direction is about 20 ion Larmor radii. As was seen in the uniform cases, the electrostatic potential Φ of the kinetic Alfvén wave propagates in phase with the vector potential A_z. The electric and magnetic fields in the region adjacent to the antenna are larger in magnitude than the wave fields generated in the resonance layer. The wave at the edge has the same features as the resonant wave. Both propagate in the y-direction with the antenna current with the same phase structure between the components of the electric and magnetic fields. This wave that forms adjacent

to the antenna is probably a sheath phenomenon. The formation of electrostatic sheaths around an antenna for the lower hybrid frequencies has been investigated by Decyk and Dawson[22,23] using a $2\frac{1}{2}D$ electrostatic particle simulation code. It is also possible that the nonuniformity does not sufficiently remove the plasma parameters from the resonance regime for nonresonant behavior to occur. The analysis is complicated by the particle reflections that occur at the boundaries.

The spatially averaged distribution function for the parallel electron velocity shown at different times in Fig. 15 exhibits flattening near the parallel wave phase velocity at the later times. The alteration of the local electron velocity function within the mode conversion region should undoubtedly be greater than what is seen in Fig. 15. We believe that the decline of the wave fields after $3\frac{1}{2}$ wave periods is related to the local change in the electron velocity distribution function. This modification from its initial state changes the plasma properties from what can be expected in the linear regime.

As was seen earlier, the kinetic Alfvén wave generated by the antenna also heats electrons. Electron temperature profiles in x are shown in Fig. 16. A broad maximum of the electron temperature develops within the mode conversion region. The largest increase occurs in the region immediately adjacent to the antenna with a smaller increase seen near the opposite (left) boundary. The rate of heating in the resonance region slows from $\omega_{pe}t = 24000$ to $\omega_{pe}t = 36000$ compared to times prior to $\omega_{pe}t = 24000$. This coincides with the decrease of the mode coverted wave fields. The temperature peak in the center of the simulation at $\omega_{pe}t = 24000$ broadens in the x-direction as time progresses, due to the diffusion of particles.

The temperature increase in the mode conversion region will be compared with the theoretical formula Eq. (11). This must be carefully done because the calculation of the heating rate from Landau damping assumes that a single coherent wave interacts linearly

with the plasma. We shall evaluate the expression

$$\frac{1}{T_e}\frac{dT_e}{dt} = \frac{\delta_e}{U_e}\frac{\omega_{pe}^2}{\omega}\int_{x_1}^{x_2}\int_0^{L_y}\frac{|E_\parallel(x,y)|^2}{8\pi}dxdy \tag{12}$$

over the range $24\Delta \leq x \leq 35\Delta$ until time $\omega_{pe}t = 24000$. The electric field values stored in the correlation data include the thermal fluctuations as well as the coherent wave. The inclusion of these fields in Eq. (12) yields an increase far in excess of the actual temperature increase since these fields do not on average contribute to electron heating. To minimize these contributions, the parallel electric field is Fourier transformed to k-space. All of the k-components of the parallel electric field are set to zero except the $(k_x, k_y = k_A)$ modes. The parallel electric field is subsequently inverse Fourier transformed back to configuration space. For the grid points located in the area between $24.5\Delta < x < 35.5\Delta$, the measured average increase of the electron temperature from $\omega_{pe}t = 0$ to $\omega_{pe}t = 24000$ is 19%. The predicted temperature increase from a summation over all the grid points within that region using the k-filtered parallel electric field is 28% agreeing reasonably well with the simulation. One reason that the computed estimate is larger than the simulation value is that the modification of the electron velocity distribution function may already slow the heating from what is expected from a linear calculation. Another reason is that the k-space filtering may not remove all of the thermal contribution to the parallel electric field.

The time evolution of the total electromagnetic field energy displayed in Fig. 17 verifies the decline in field energy after $\omega_{pe}t = 20000$ indicated in Fig. 14. The field energy does not show any dramatic increases above initial values. The ion kinetic energy undergoes a rapid increase during the first wave period as the kinetic Alfvén wave establishes itself and increases linearly afterwards. There is an energy exchange again between the ions and the field energy clearly seen towards the completion of the run. This energy exchange has a frequency that is 1.5 times the pump frequency in contrast to twice the value observed in

the periodic simulations. The increase of the ion temperatures are reasonably explained by $\mathbf{E} \times \mathbf{B}$ oscillations. Some true thermalization occurs from the phase mixing caused by ion reflections at the boundaries.

The total electron kinetic energy increases most rapidly from times $\omega_{pe}t = 9000$ to $\omega_{pe}t = 15000$. The heating rate then undergoes a subsequent decline until $\omega_{pe}t = 22000$, after which it increases more slowly. The rate of electron heating slows as the electron velocity distribution function flattens. The decline in the electromagnetic field energy also correlates well with the decrease in the electron heating rate. The total electron kinetic energy increases 13% above its initial thermal value. This value is larger than what would be experimentally measured since our measurement does not include electron thermal motion perpendicular to the magnetic field. Through the length of the run, the electrons acquire a net drift velocity that is approximately 5% of the electron thermal velocity.

2. $\mathrm{V}_A(\mathrm{x}_{res}) < \mathrm{V}_{te}$

The last example exhibits results from a nonuniform example where the plasma β in the resonance region is well above the electron-to-ion mass ratio, $\beta(x_{res})M/m = 8.6$. The parameters for the plasma at the resonance layer are the same as for case iv) of subsection B). The antenna parameters have the values $\omega_A = 1.44 \times 10^{-3}\omega_{pe}, k_A\Delta = 1.96 \times 10^{-2}$ and $W = 4.5 \times 10^{-3}$. The system is followed to $\omega_{pe}t = 19200$ which is 4.4 wave periods. From the results of the homogeneous runs, it is expected that the reaction of the plasma for this example will be weaker than seen in the previous case.

As is found in the earlier example in this section, the wave electric and magnetic fields have their largest amplitudes in the region adjacent to the antenna as can be seen from the three-dimensional graphs of field energy densities in Fig. 18. Lines running parallel to the time axis represent a spatial averaging over three grid points and lines running parallel to the x-axis are averaged over one-fourth of a period. At initial times, there is

a secondary maximum of the field energy at the left edge opposite of the antenna. As time progresses, the field energy densities, displayed in Fig. 18 decline at the left edge near $x = 0$ with a corresponding increase in amplitude near the resonance layer, which we interpret as the mode conversion of the kinetic Alfvén wave. The amplitude of this resonant wave is comparatively smaller than for the immediately preceding example. The evidence supporting the occurence of the kinetic Alfvén wave mode conversion is weaker than in the previous example but is nevertheless still convincing.

The electron velocity distribution function parallel to the magnetic field displays weak smoothing about the parallel phase velocity of the wave. The time evolution of the electromagnetic field energy does not have a net increase. The oscillations of the field energy are at approximately 1.5 times the pump frequency as is seen earlier. The ions participate very weakly if at all in these oscillations. The electrons gain energy most rapidly during the first wave period as the kinetic Alfvén wave in the resonance region establishes itself. The net trend of the total electron kinetic energy after this is still increasing but at a much slower rate. There is a small decrease of energy beginning at 2.6 periods that is reminiscent of the decline seen in the homogeneous system for these parameters. The increases in the temperatures are too small to detect spatial dependencies. The electron acquire a small net drift velocity of $\langle V_D \rangle_{||} = 0.01 V_{Te}$.

Two different parameter regimes have been examined in nonuniform systems. Mode conversion of the kinetic Alfvén wave is observed near the resonance layer for both examples. However, the amplitude of the mode converted wave is smaller than the wave fields adjacent to the antenna. The time evolution of the resonant kinetic Alfvén wave suggests that its structure is sensitive to the shape of the electron velocity distribution function. The electron temperature increase in the mode conversion region agrees reasonably well with the expectation of Landau damping. The resonance interaction for the lower β case where $V_A(x_{res}) = V_{Te}$ is stronger than for the higher β case where $V_A(x_{res}) = 0.56 V_{Te}$.

IV. SUMMARY

The kinetic processes associated with Alfvén wave resonance heating are examined in this paper. Different parameter regimes were investigated in simulations that were 1) uniform systems with both the x- and y-direction periodic and 2) nonuniform systems with the x-direction bounded and the y-direction periodic. The kinetic Alfvén wave is seen to grow well above initial levels. Electron heating and a net electron current are produced by the kinetic Alfvén wave. The mechanism has been identified as Landau damping. The observed increase in the ion kinetic energy is caused by $\mathbf{E} \times \mathbf{B}$ drifts driven by the wave electrostatic fields. A large portion of the total wave energy resides in the ion sloshing motion. If some mechanism exists to disrupt the phase of (i.e., stochasticize) the ion motion with respect to the wave fields, a net thermalization of the ions results. This seems to occur in the bounded simulations from particle reflections at the boundaries over a long simulation run.

The Landau damping of the electrons progressed to a nonlinear stage where the electron velocity distribution function parallel to the magnetic field flattened about the parallel phase velocity of the wave. This alteration of the electron velocity distribution function has been correlated with a decline in the magnitude of the kinetic Alfvén wave in the resonance region and with a slow-down in the rate of electron heating. Most of the theoretical work is based on the assumption that the absorption of wave energy does not significantly change the plasma behavior. However, our simulation results demonstrate that the plasma heating can alter the properties of the Alfvén wave when the local electron heating increases 5-10%. In contrast, the TCA tokamak reports gains of 25% in the bulk electron temperature. However, a wide band resonance might be able to prevent the original distribution function from the severe distortions observed in our simulations. One must be aware that the simulation operates with much higher power densities than currently exist in

present experimental devices. Thermalization processes would guide the electron velocity distribution function back to Maxwellian more effectively in the experiments. There does exist experimental evidence of nonlinear behavior associated with the Alfvén wave heating scheme. For example, it has been observed on the PRETEXT tokamak by T. Evans[25] that the electron density fluctuations reach a saturation level, $\tilde{n}_e/n_{e0} \sim 0.6\%$, in power scaling measurements. We therefore surmise that nonlinear effects from the absorption of wave energy can modify the mode structures and wave propagation as well as heating rates and suggest this as an area for further theoretical and experimental investigation.

ACKNOWLEDGEMENTS

We would like to thank Dr. Dave Ross, Dr. Swadesh Mahajan, and Professor Roger Bengtson for helpful and enlightening discussions. This work was supported by the U. S. Department of Energy grant *DE*-FG05-80ET53088 and National Science Foundation grant ATM85-06646.

References

1. A.A. Tataronis and W. Grossman, Z. Physic **16**, 667 (1973).
2. A. Hasegawa and L. Chen, Phys. Rev. Lett. **32**, 454 (1974).
3. R. A. Smith, C. K. Goertz, and W. Grossman, Geophys. Res. Lett. **13**, 1380 (1986).
4. C. K. Goertz, Planet. Spac. Sci. **32**, 1387 (1984).
5. J. A. Ionson, Astrophys. J. **226**, 650 (1978).
6. A. Hasegawa and L. Chen, Phys. Fluids **19**, 1924 (1976).
7. D.W. Ross, G.L. Chen and S.M. Mahajan, Phys. Fluids **25**, 652 (1982).
8. B. Balet, K. Appert and J. Vaclavik, Plasma Phys. **24**, 1005 (1982).
9. K. Appert, R. Gruber, F. Troyon, and J. Vaclavik, Plasma Phys. **24**, 1147 (1982).
10. K. Appert, B. Balet, R. Gruber, F. Troyon, T. Tsunematsu, and J. Vaclavik, Nucl. Fus. **22**, 903 (1982).
11. K. Appert and J. Vaclavik, Plasma Phys. **25**, 551 (1983).
12. T. Obiki, T. Mutoh, S. Adachi, A. Sasaki, A. Iiyoshi, and K. Uo, Phys. Ref. Lett. **39**, 812 (1977).
13. A. deChambrier, A.D. Cheetham, A. Heym, F. Hofmann, B. Joye, R. Keller, A. Lietti, J.B. Lister, and A. Pochelon, Plasma Phys. **24**, 893 (1982).
14. A. deChambrier, A. Heym, F. Hofmann, B. Joye, R. Keller, A. Lietti, J.B. Lister, P.D. Morgan, M.J. Peacock, A. Pochelon, and M.F. Stap, Plasma Phys. **25**, 1021 (1983).
15. K. Appert, G.A. Collins, F. Hofmann, R. Keller, A. Lietti, J.B. Lister, A. Pochelon, and L. Villard, Phys. Rev. Lett. **54**, 1671 (1985).
16. T.E. Evans, P.M. Valanju, J.F. Benesch, Roger D. Bengtson, Y-M. Li, S.M. Mahajan, M.F. Oakes, D.W. Ross, X-Z. Wang, J.G. Watkins, and C.M. Surko, Phys. Rev. Lett. **53**, 1743 (1984).
17. F.D. Witherspoon, S.C. Prager and J.C. Sprott, Phys. Rev. Lett. **53**, 1559 (1984).
18. J.L. Geary, T.T. Tajima, J.N. Leboeuf, E.G. Zaidman, and J.H. Han, Comp. Phys. Comm. **42**, 313 (1986).
19. M. Tanaka, T. Sato, and A. Hasegawa, Geophys. Res. Lett. **14**, 868 (1987).
20. W.W. Lee, M.S. Chance and H. Okuda, Phys. Rev. Lett. **46**, 1675 (1981); W.W. Lee, H. Okuda and W.M. Nevins, in: Proc. Eight Conf. on Numerical Simulation of Plasmas,

Lawrence Livermore Laboratory Report No. CONF-780614 (1978) p. PD.7.

21. H. Naitou, S. Tokuda and T. Kamimura, J. Comp. Phys. **33**, 86 (1979).

22. V.K. Decyk, J.M. Dawson and G.J. Morales, Phys. Fluids **22**, 507 (1979).

23. V.K. Decyk, G.J. Morales and J.M. Dawson, Phys. Fluids **23**, 826 (1980).

24. T.H. Stix, *2nd International Symposium on Heating in Toroidal Plasmas* (Cuomo, Italy, 1980).

25. T.E. Evans, Ph.D dissertation, Physics Department, University of Texas at Austin (1984).

Figure Captions

Fig. 1 Time evolution of (a) total electromagnetic field energies, (b) total ion kinetic energies, and (c) total electron kinetic energies ending at $\omega_{pe}t = 13000$ for case 1 of subsection B. The wave driven by the antenna does not match any plasma resonance.

Fig. 2 Contour plots of the fields (a) B_x, (b) B_y, and (c) E_{Tz} at $\omega_{pe}t = 24000$ for case 2 of subsection B. The driven wave matches the Alfvén resonance and $V_A = V_{Te}$.

Fig. 3 Contour plots of the fields (a) E_{Lx} and (b) E_{Ly} at $\omega_{pe}t = 24000$ for case 2 of subsection B. The electrostatic fields are entirely due to the plasma response.

Fig. 4 Electron velocity distribution function parallel to the magnetic field at (a) $\omega_{pe}t = 0$ and (b) $\omega_{pe}t = 36000$ for case 2 of subsection B. The distribution function flattens about the phase velocity of the wave.

Fig. 5 Time evolution of (a) total electromagnetic field energies, (b) total ion kinetic energies, and (c) total electron kinetic energies ending at $\omega_{pe}t = 36000$ for case 2 of subsection B.

Fig. 6 Contour plots of the fields (a) B_x, (b) B_y, and (c) E_{Tz} at $\omega_{pe}t = 19200$ for case 3 of subsection B. The wave phase velocity, V_A, is less than V_{Te}. By this time, the growth has saturated creating a distortion of the wave fields from their initial slopes.

Fig. 7 The electron velocity distribution function at times (a) $\omega_{pe}t = 0.0$, (b)$\omega_{pe}t = 12000$, and (c)$\omega_{pe}t = 24000$ for case 3 of subsection B also exhibits smoothing about the phase velocity.

Fig. 8 Time evolution of (a) total electromagnetic field energies, (b) total ion kinetic energies, and (c) total electron kinetic energies ending at $\omega_{pe}t = 24000$ for case 3 of subsection B.

Fig. 9 Contour plots of the fields (a) B_x, (b) B_y, and (c) E_{Tz} at $\omega_{pe}t = 16000$ for case 4 of subsection B. Strong currents modify the electromagnetic field contours.

Fig. 10 Electron velocity distribution function parallel to the magnetic field at (a)

$\omega_{pe}t = 0$ and (b) $\omega_{pe}t = 16000$ for case 4 of subsection B. The wave traps electrons and creates a tail on the distribution function.

Fig. 11 Phase space scatter plots, $x - V_{e\|}$, of electrons at (a) $\omega_{pe}t = 0$ and (b) $\omega_{pe}t = 16000$ for case 4 of subsection B. The trapping is strongest in the vicinity of the antenna and is strong where the accelerating electric fields experience a secondary maximum.

Fig. 12 Time evolution of (a) total electromagnetic field energies, (b) total ion kinetic energies, and (c) total electron kinetic energies ending at $\omega_{pe}t = 16000$ for case 4 of subsection B.

Fig. 13 Spatial variation of the Alfvén speed V_A for the two simulations of a nonuniform plasma.

Fig. 14 Spatial dependence and temporal evolution of the field energy densities (a) $|E_{Tz}(x, k_A, t)|^2$, (b) $|B_x(x, k_A, t)|^2$ and (c) $|E_{Ly}(x, k_A, t)|^2$ from different perspectives ending at $\omega_{pe}t = 54000$ for for case 1 of subsection C highlight the growth, saturation, and subsequent decline of the Alfvén wave at the resonance layer.

Fig. 15 Electron velocity distribution function parallel to the magnetic field at (a) $\omega_{pe}t = 0$, (b) $\omega_{pe}t = 12000$, (c) $\omega_{pe}t = 24000$, and d) $\omega_{pe}t = 36000$ for case 1 of subsection C exhibits flattening at the wave phase velocity.

Fig. 16 Spatial dependence of the electron temperature at (a) $\omega_{pe}t = 0$, (b) $\omega_{pe}t = 12000$, (c) $\omega_{pe}t = 24000$, and d) $\omega_{pe}t = 36000$ for case 1 of subsection C shows electron heating in the resonance region and adjacent to the antenna.

Fig. 17 Time evolution of the (a) total electromagnetic field energies, (b) total ion kinetic energies, and (c) total electron kinetic energies ending at $\omega_{pe}t = 54000$ for case 1 of subsection C.

Fig. 18 Spatial dependence and temporal evolution of the field energy densities (a) $|B_x(x, k_A, t)|^2$, (b) $|E_{Ly}(x, k_A, t)|^2$, and (c) $|E_{Tz}(x, k_A, t)|^2$ from different perspectives ending at $\omega_{pe}t = 19200$ for case 2 of subsection C show the development of the shear Alfvén wave at a lower amplitude than the previous nonuniform case.

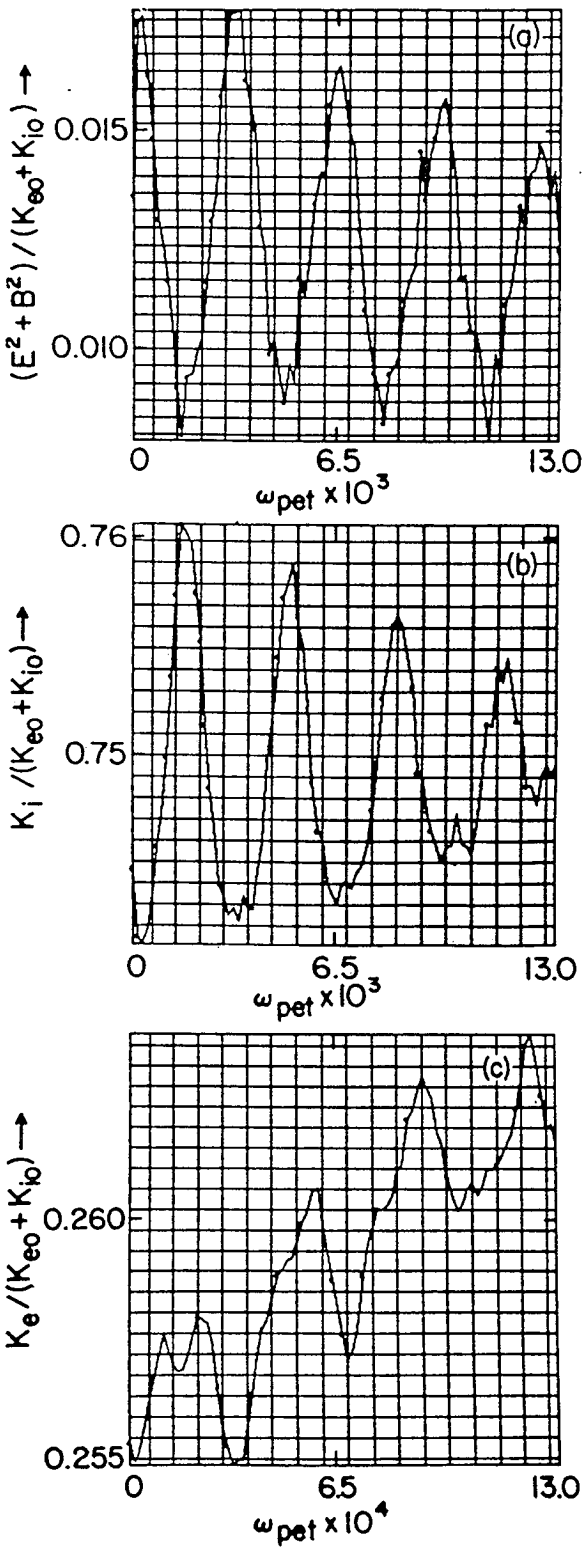
(a)
$(E^2+B^2)/(K_{eo}+K_{io})\rightarrow$
0.015
0.010
0
6.5
13.0
$\omega_{pet} \times 10^3$
(b)
$K_i/(K_{eo}+K_{io})\rightarrow$
0.76
0.75
0
6.5
13.0
$\omega_{pet} \times 10^3$
(c)
$K_e/(K_{eo}+K_{io})\rightarrow$
0.260
0.255
0
6.5
13.0
$\omega_{pet} \times 10^4$

Fig. 1

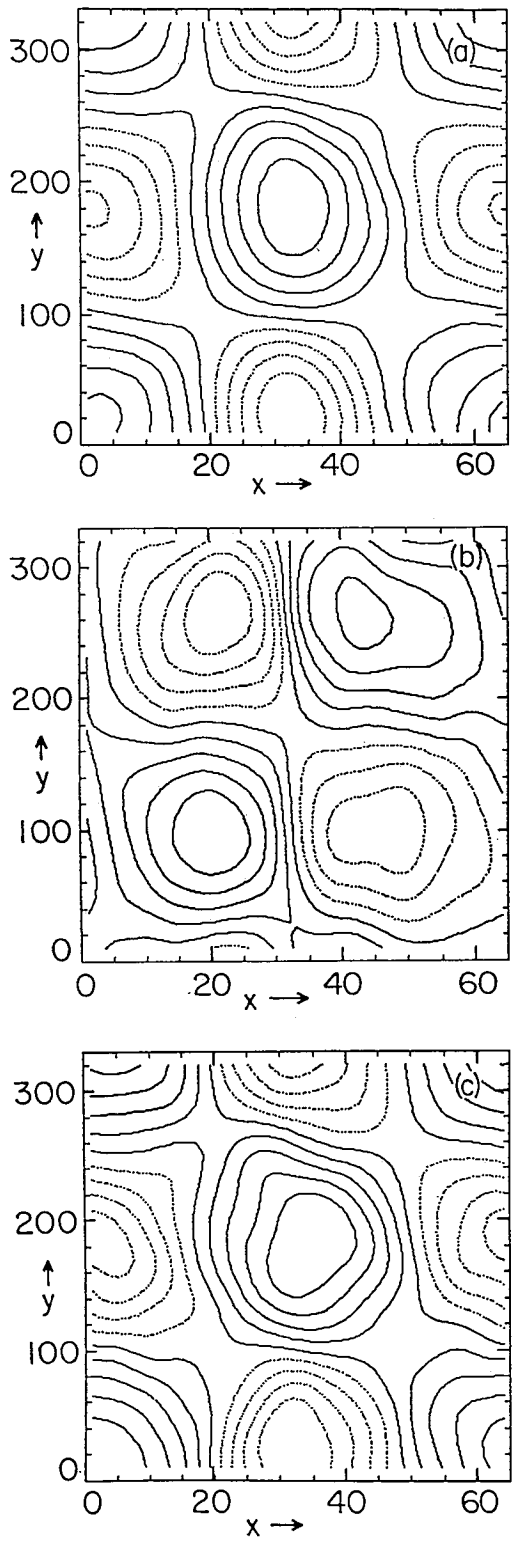
(a)
300
200
y
100
0
0
20
40
60
x
(b)
300
200
y
100
0
0
20
x
40
60
(c)
300
200
y
100
0
0
20
40
60
x

Fig. 2

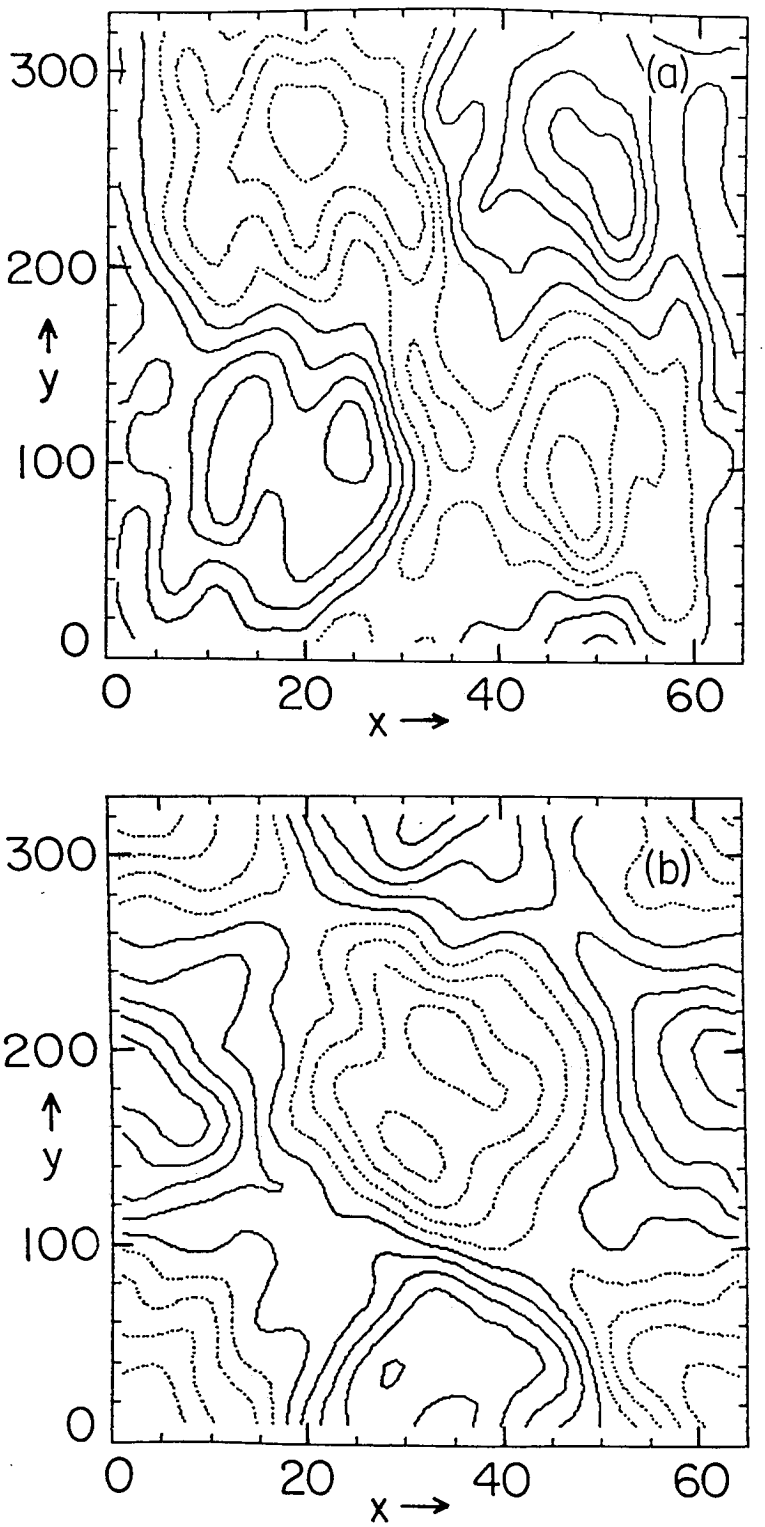

Fig. 3

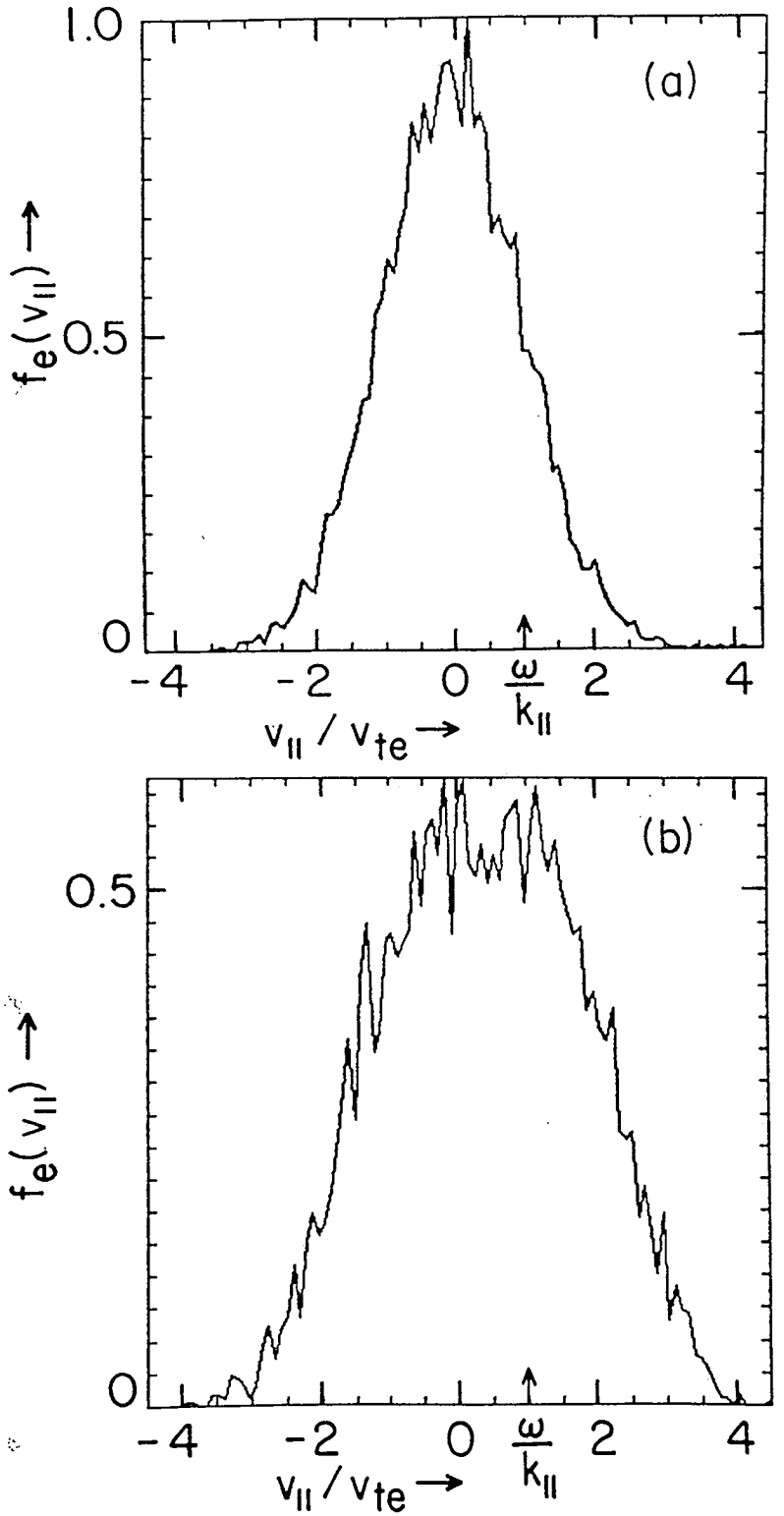
1.0
0.5
0
(a)
$f_e(v_{||})$ →
-4
-2
0
$\frac{\omega}{k_{||}}$
2
4
$v_{||} / v_{te}$ →
0.5
0
(b)
$f_e(v_{||})$ →
-4
-2
0
$\frac{\omega}{k_{||}}$
2
4
$v_{||} / v_{te}$ →

Fig. 4

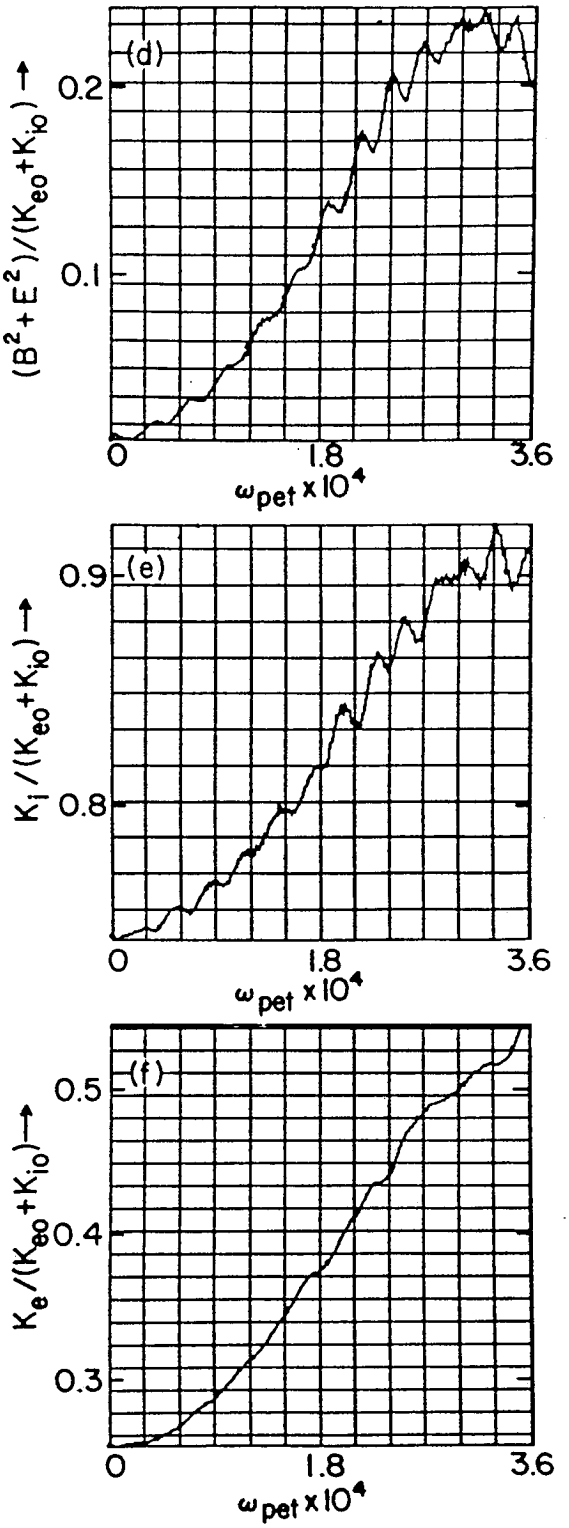
(d)
$(B^2+E^2)/(K_{eo}+K_{io})\rightarrow$
0.2
0.1
0
1.8
3.6
$\omega_{pet} \times 10^4$
(e)
$K_i/(K_{eo}+K_{io})\rightarrow$
0.9
0.8
0
1.8
3.6
$\omega_{pet} \times 10^4$
(f)
$K_e/(K_{eo}+K_{io})\rightarrow$
0.5
0.4
0.3
0
1.8
3.6
$\omega_{pet} \times 10^4$

Fig. 5

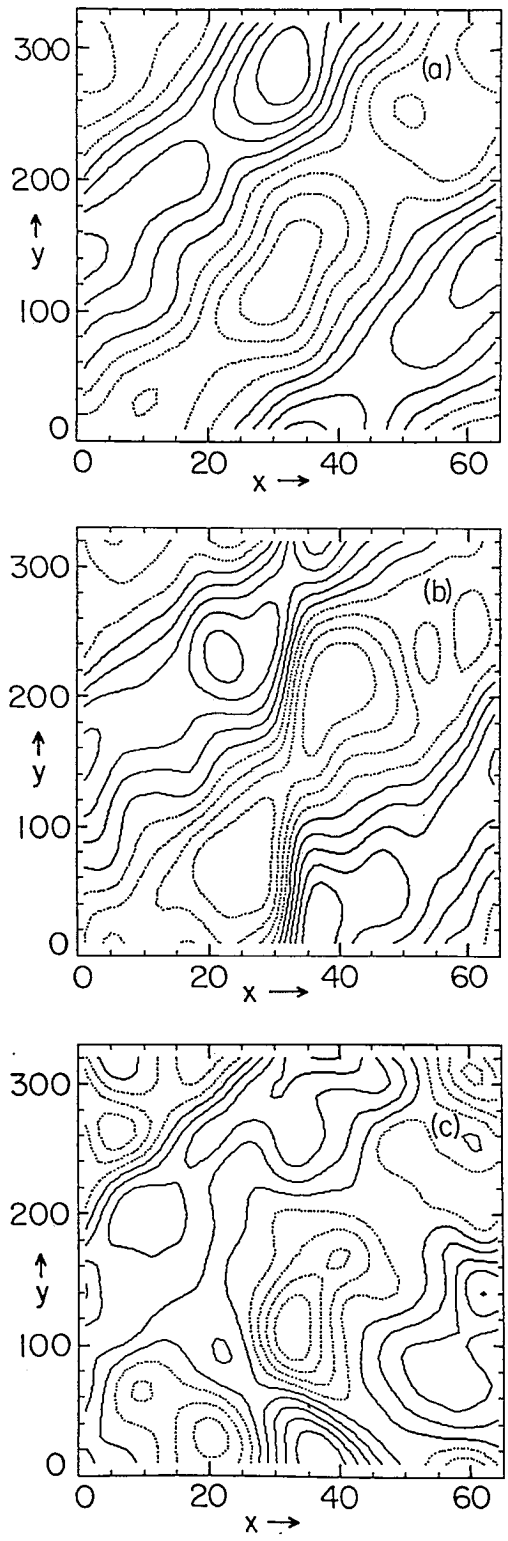

Fig. 6

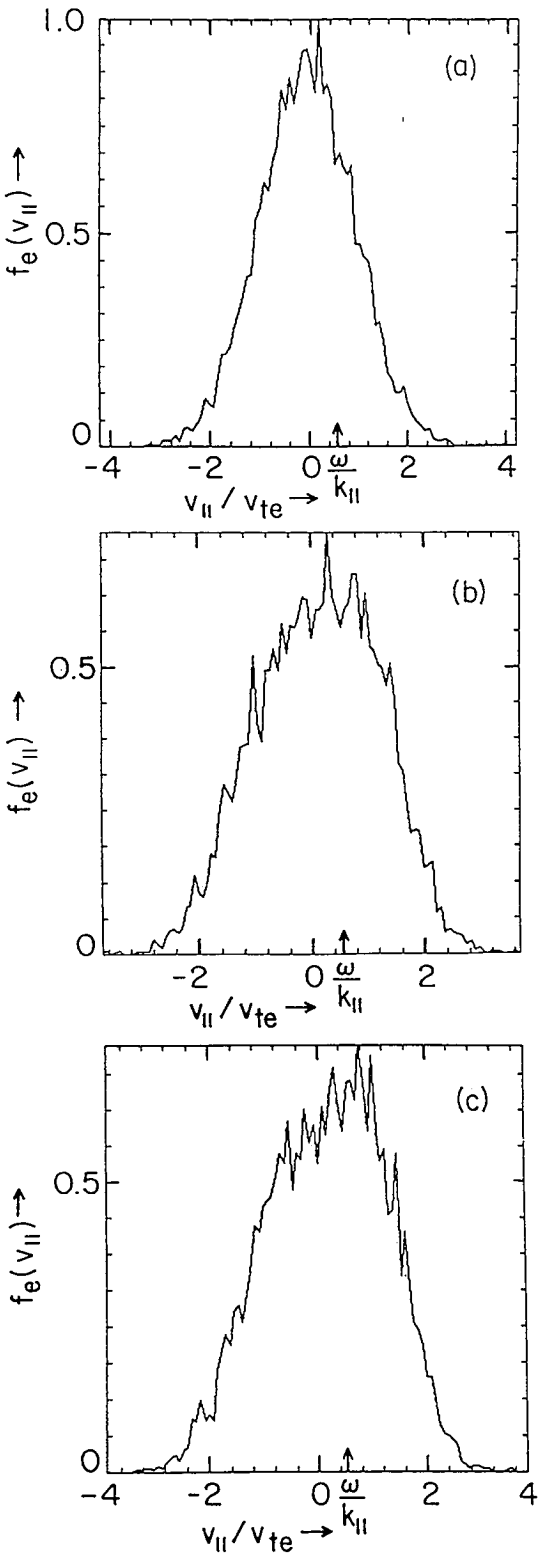
1.0
0.5
0
(a)
$f_e(v_{||}) \rightarrow$
-4
-2
0
$\frac{\omega}{k_{||}}$
2
4
$v_{||} / v_{te} \rightarrow$
(b)
0.5
0
-2
0
$\frac{\omega}{k_{||}}$
2
$f_e(v_{||}) \rightarrow$
$v_{||} / v_{te} \rightarrow$
(c)
0.5
0
-4
-2
0
$\frac{\omega}{k_{||}}$
2
4
$f_e(v_{||}) \rightarrow$
$v_{||} / v_{te} \rightarrow$

Fig. 7

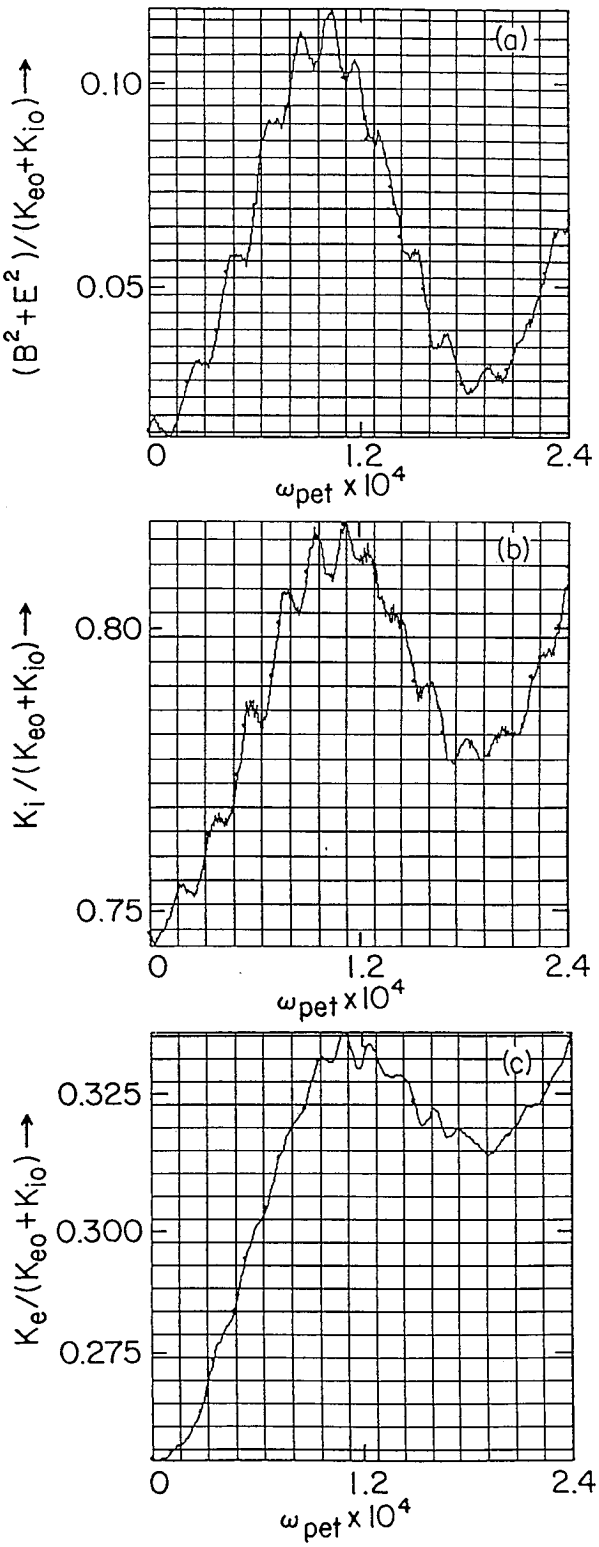
(a)
0.10
0.05
$(B^2+E^2)/(K_{eo}+K_{io})\rightarrow$
0
1.2
2.4
$\omega_{pet} \times 10^4$
(b)
0.80
0.75
$K_i/(K_{eo}+K_{io})\rightarrow$
0
1.2
2.4
$\omega_{pet} \times 10^4$
(c)
0.325
0.300
0.275
$K_e/(K_{eo}+K_{io})\rightarrow$
0
1.2
2.4
$\omega_{pet} \times 10^4$

Fig. 8

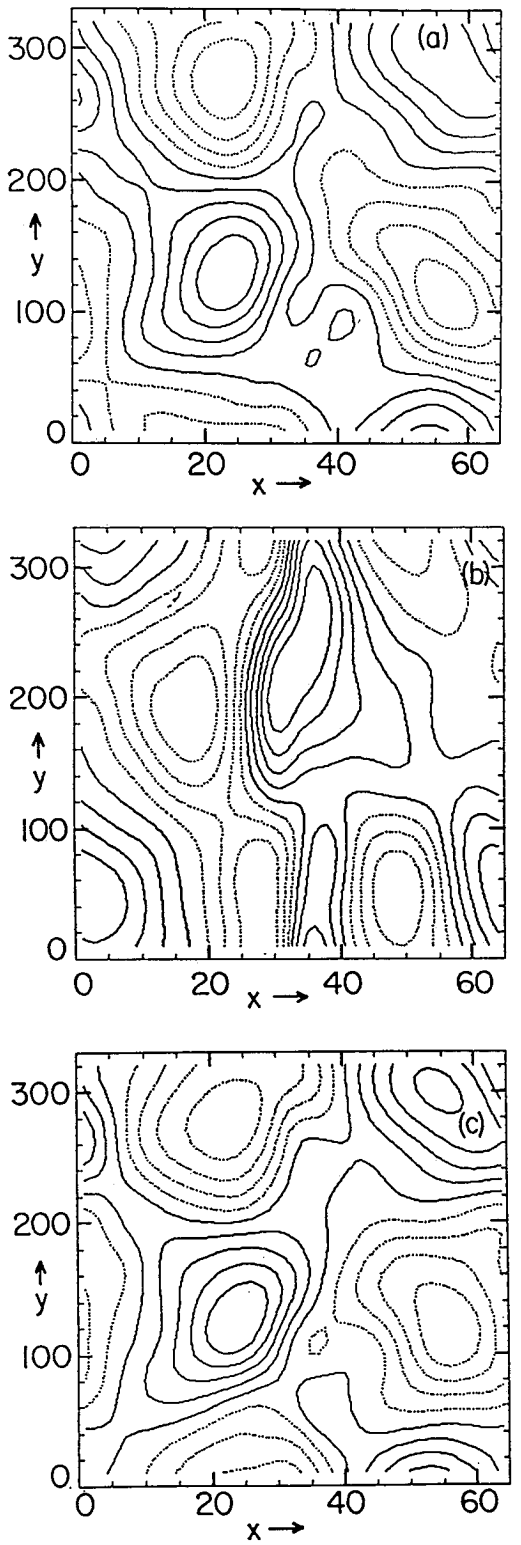
(a)
300
200
100
0
y
0
20
40
60
x
(b)
300
200
100
0
y
0
20
40
60
x
(c)
300
200
100
0
y
0
20
40
60
x

Fig. 9

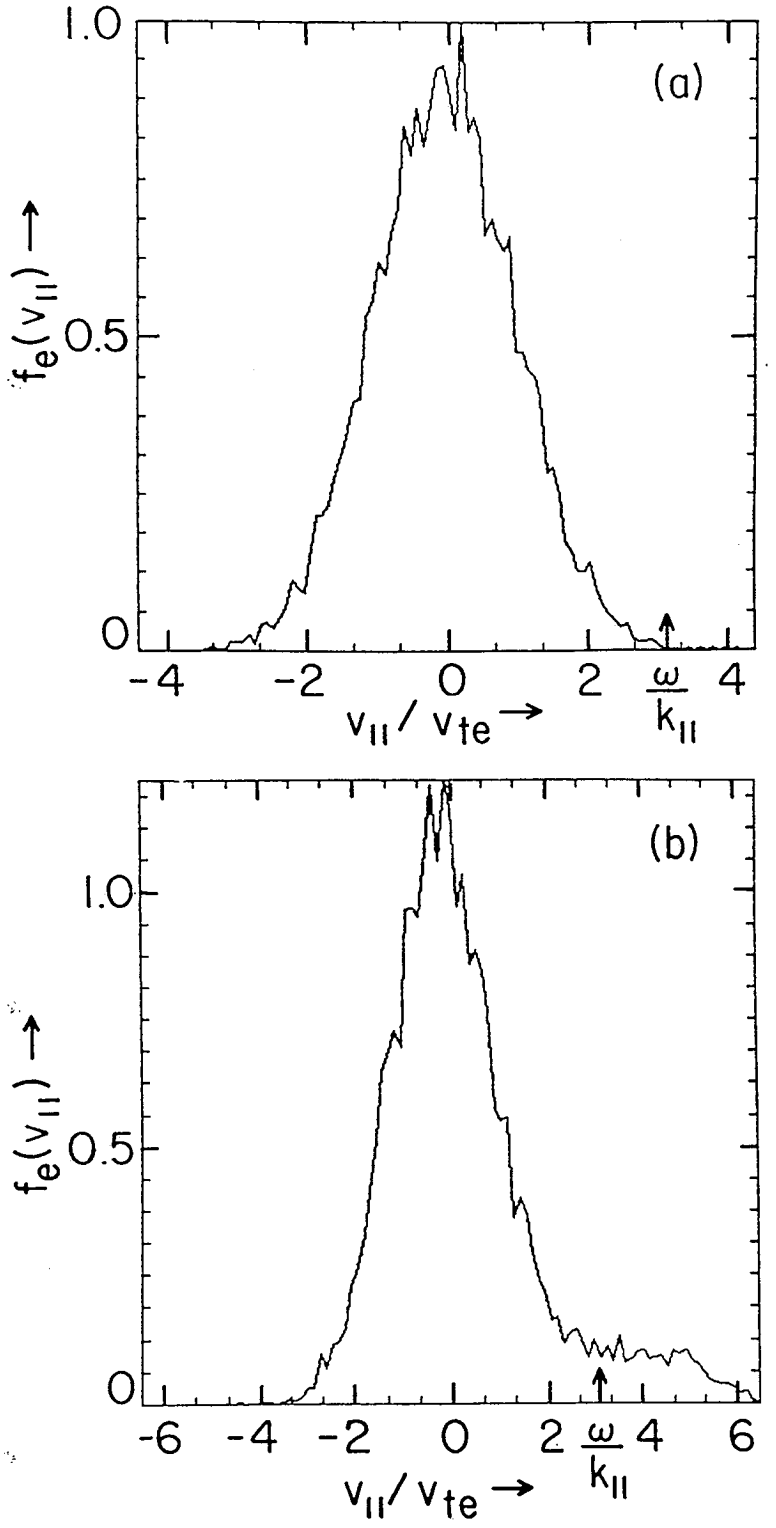
1.0
0.5
0
(a)
$f_e(v_{||})$ →
-4
-2
0
2
$\frac{\omega}{k_{||}}$
4
$v_{||}/v_{te}$ →
1.0
0.5
0
(b)
$f_e(v_{||})$ →
-6
-4
-2
0
2
$\frac{\omega}{k_{||}}$
4
6
$v_{||}/v_{te}$ →

Fig. 10

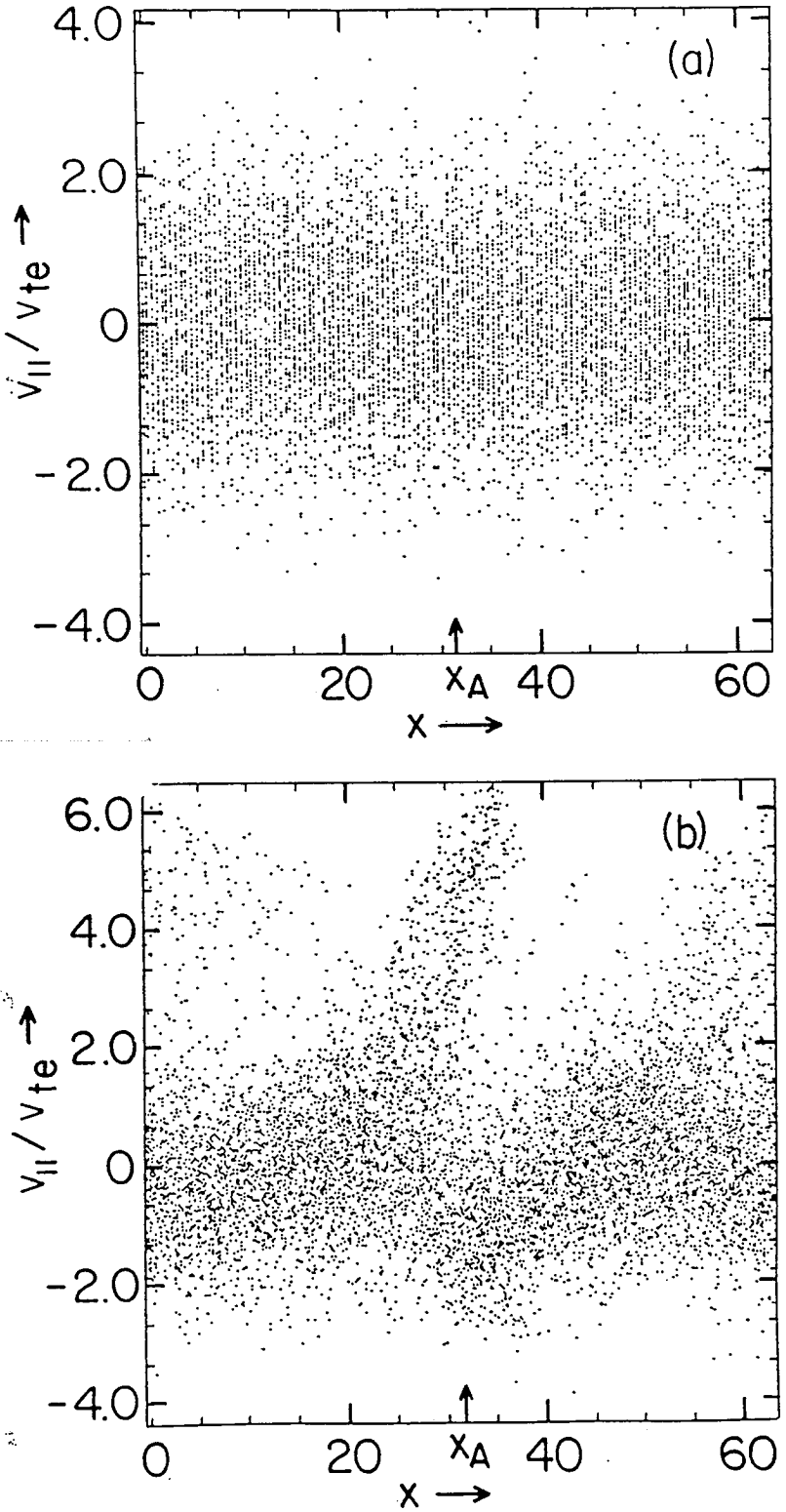
(a)
4.0
2.0
0
-2.0
-4.0
$v_{||} / v_{te}$
0
20
x_A
40
60
x
(b)
6.0
4.0
2.0
0
-2.0
-4.0
$v_{||} / v_{te}$
0
20
x_A
40
60
x

Fig. 11

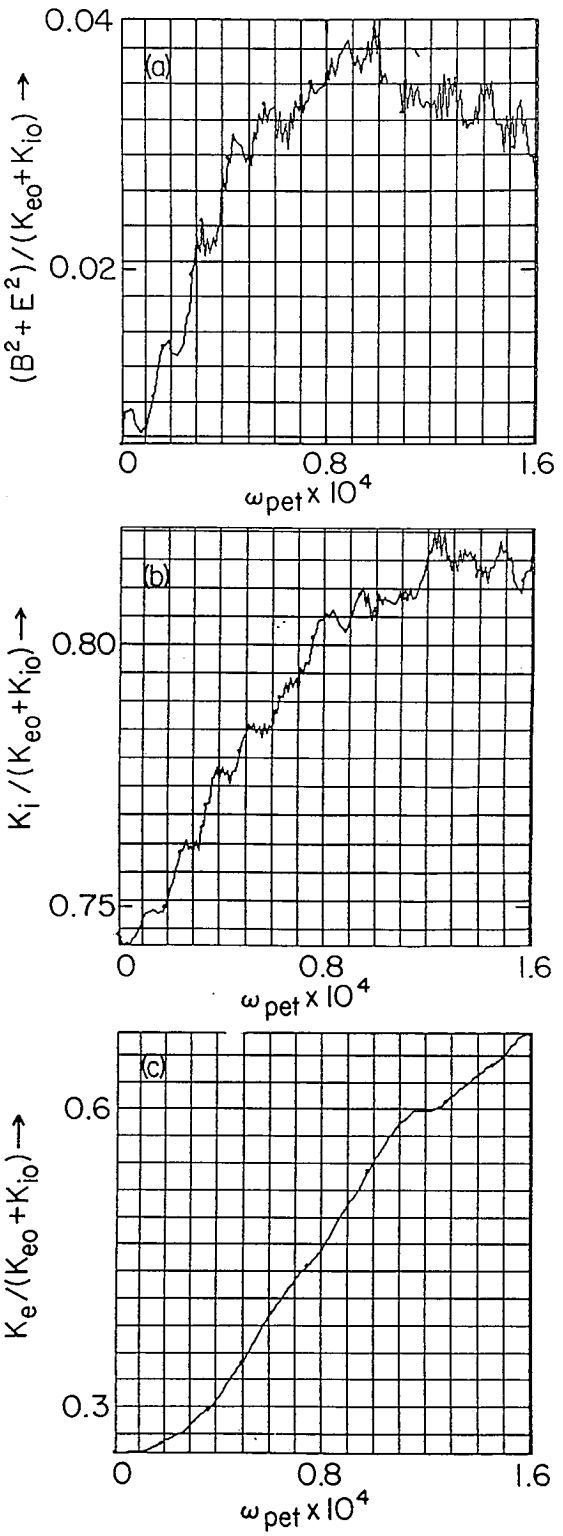
0.04
0.02
(a)
$(B^2+E^2)/(K_{eo}+K_{io})\rightarrow$
0
0.8
1.6
$\omega_{pet} \times 10^4$
0.80
0.75
(b)
$K_i/(K_{eo}+K_{io})\rightarrow$
0
0.8
1.6
$\omega_{pet} \times 10^4$
0.6
0.3
(c)
$K_e/(K_{eo}+K_{io})\rightarrow$
0
0.8
1.6
$\omega_{pet} \times 10^4$

Fig. 12

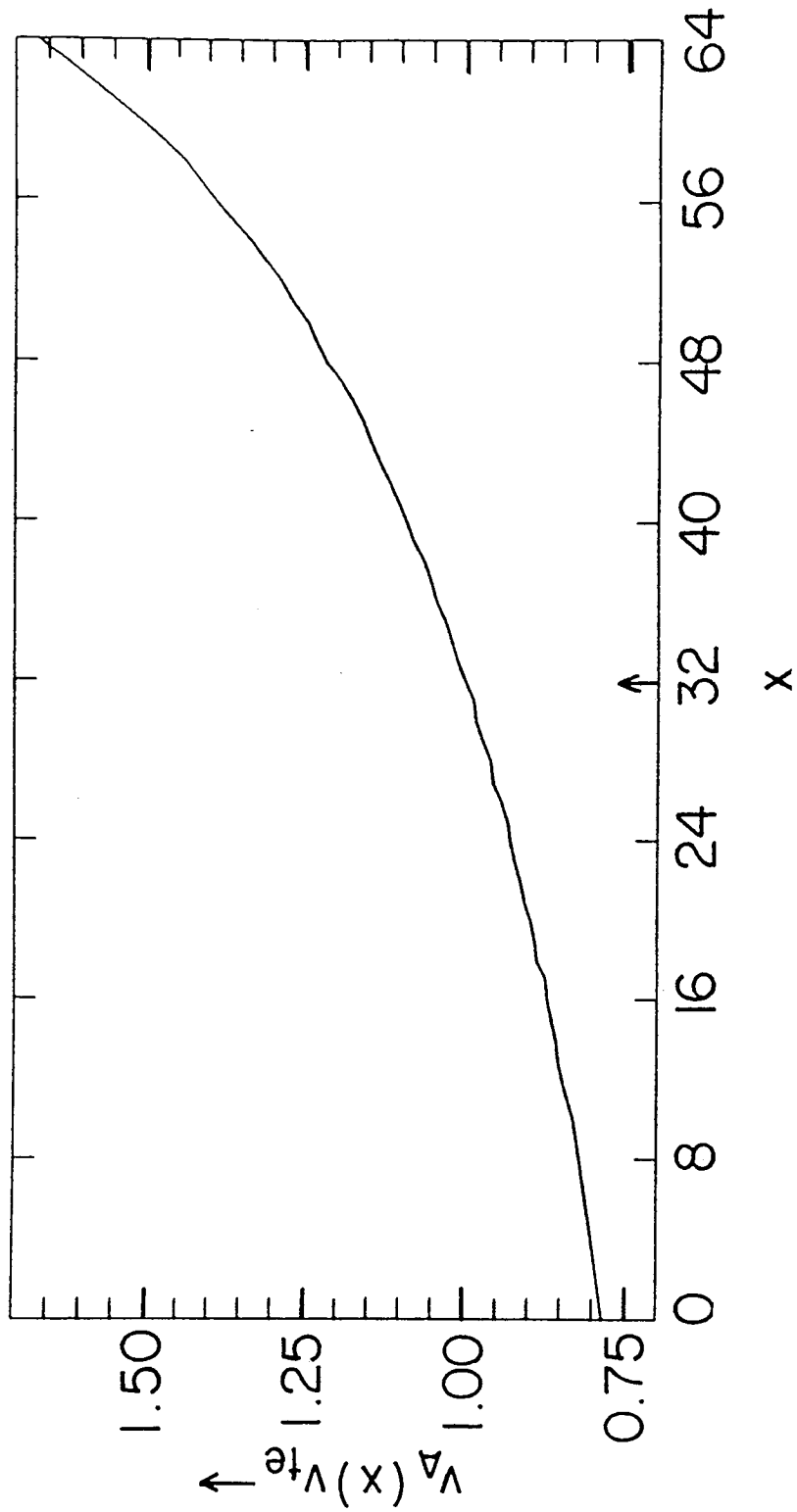

Fig. 13

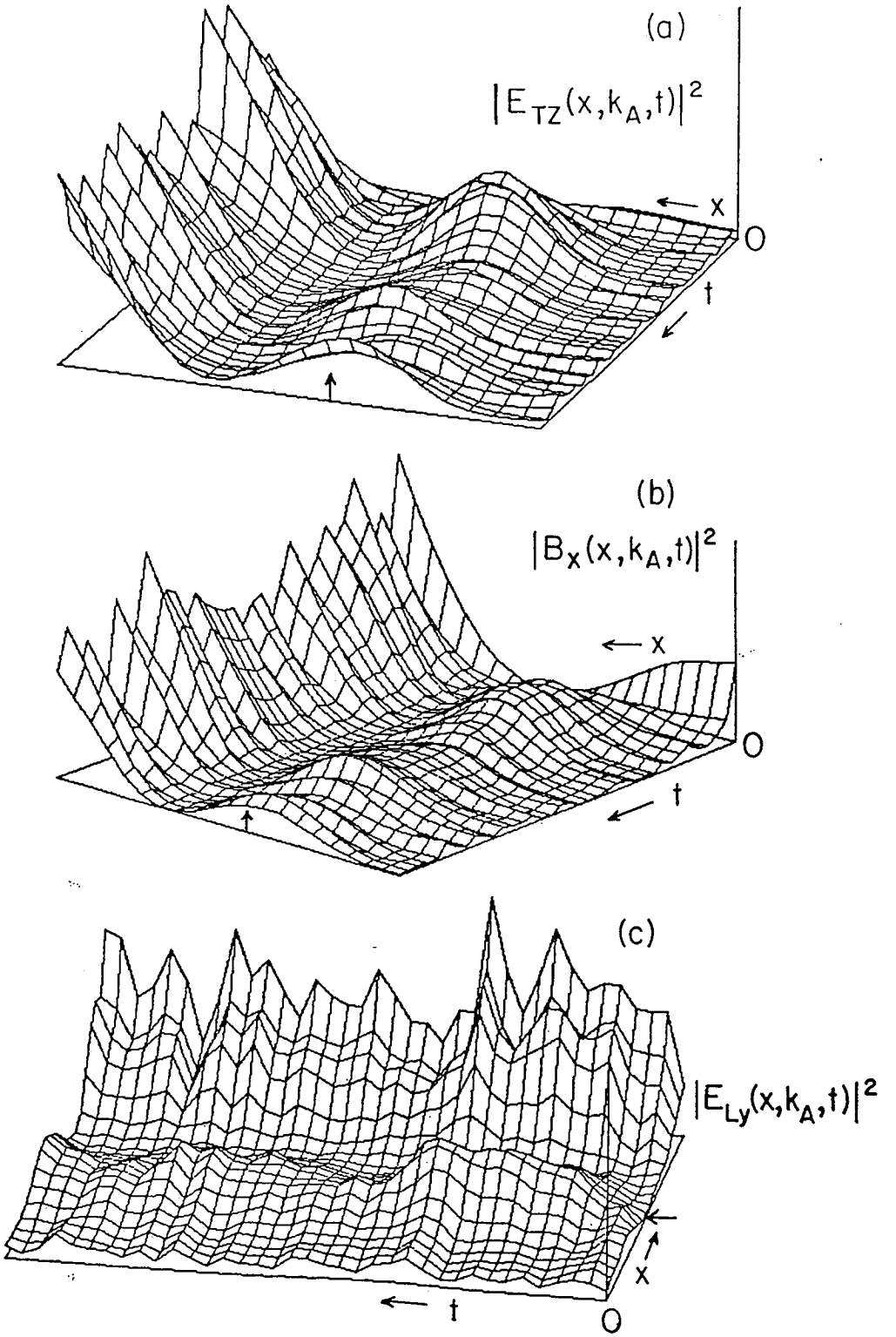

Fig. 14

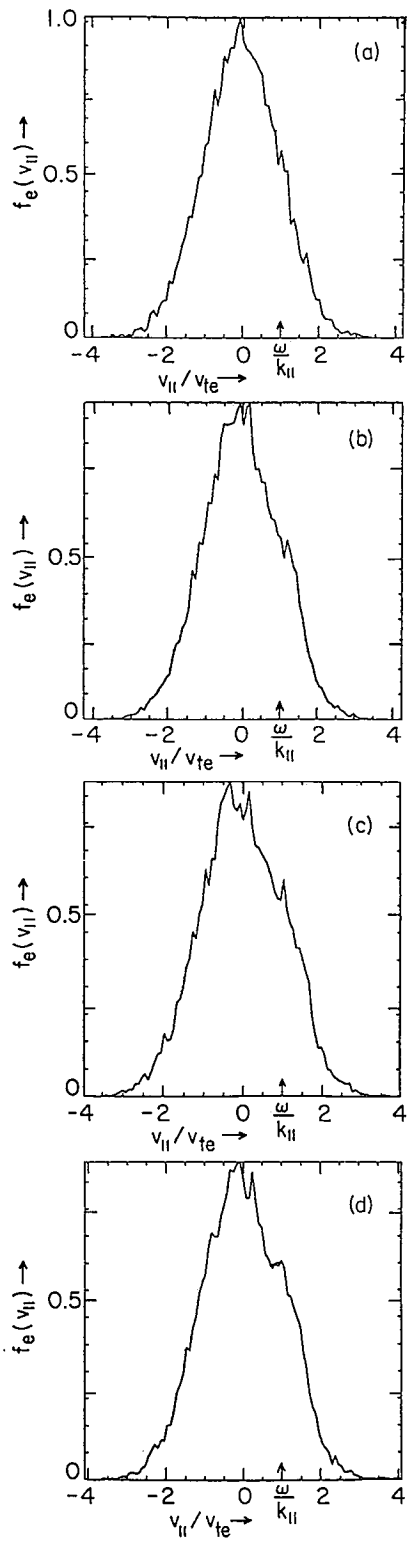

Fig. 15

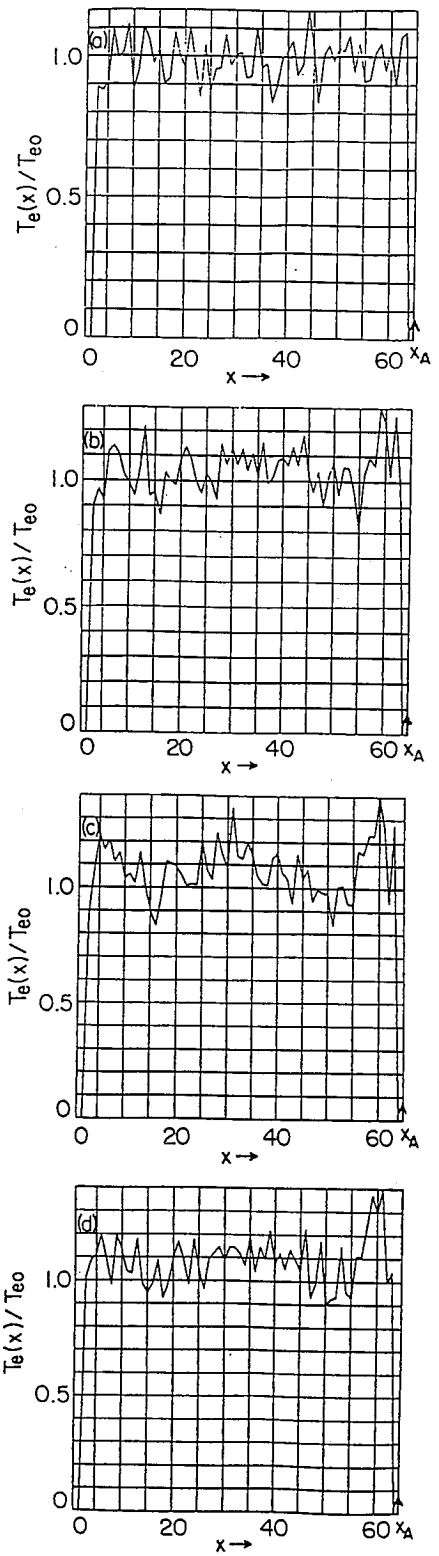

Fig. 16

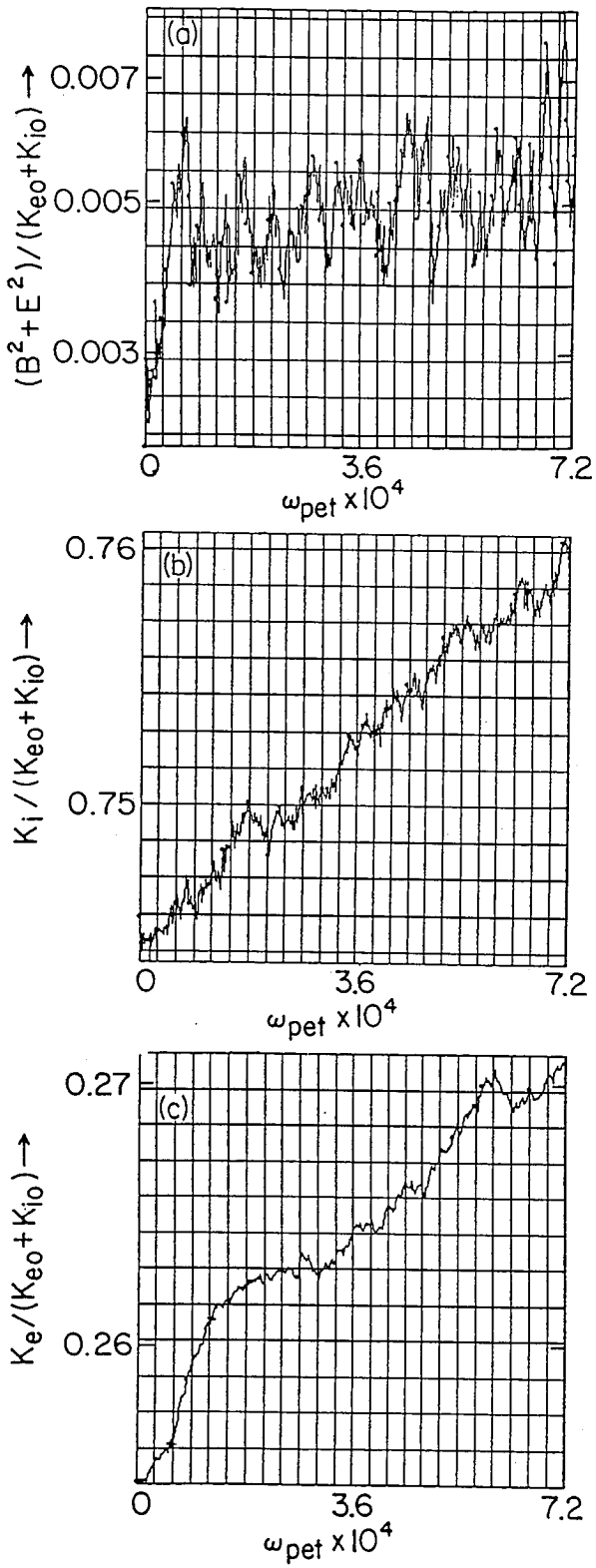
(a)
0.007
0.005
0.003
$(B^2+E^2)/(K_{eo}+K_{io})\rightarrow$
0
3.6
7.2
$\omega_{pet} \times 10^4$
(b)
0.76
0.75
$K_i/(K_{eo}+K_{io})\rightarrow$
0
3.6
7.2
$\omega_{pet} \times 10^4$
(c)
0.27
0.26
$K_e/(K_{eo}+K_{io})\rightarrow$
0
3.6
7.2
$\omega_{pet} \times 10^4$

Fig. 17

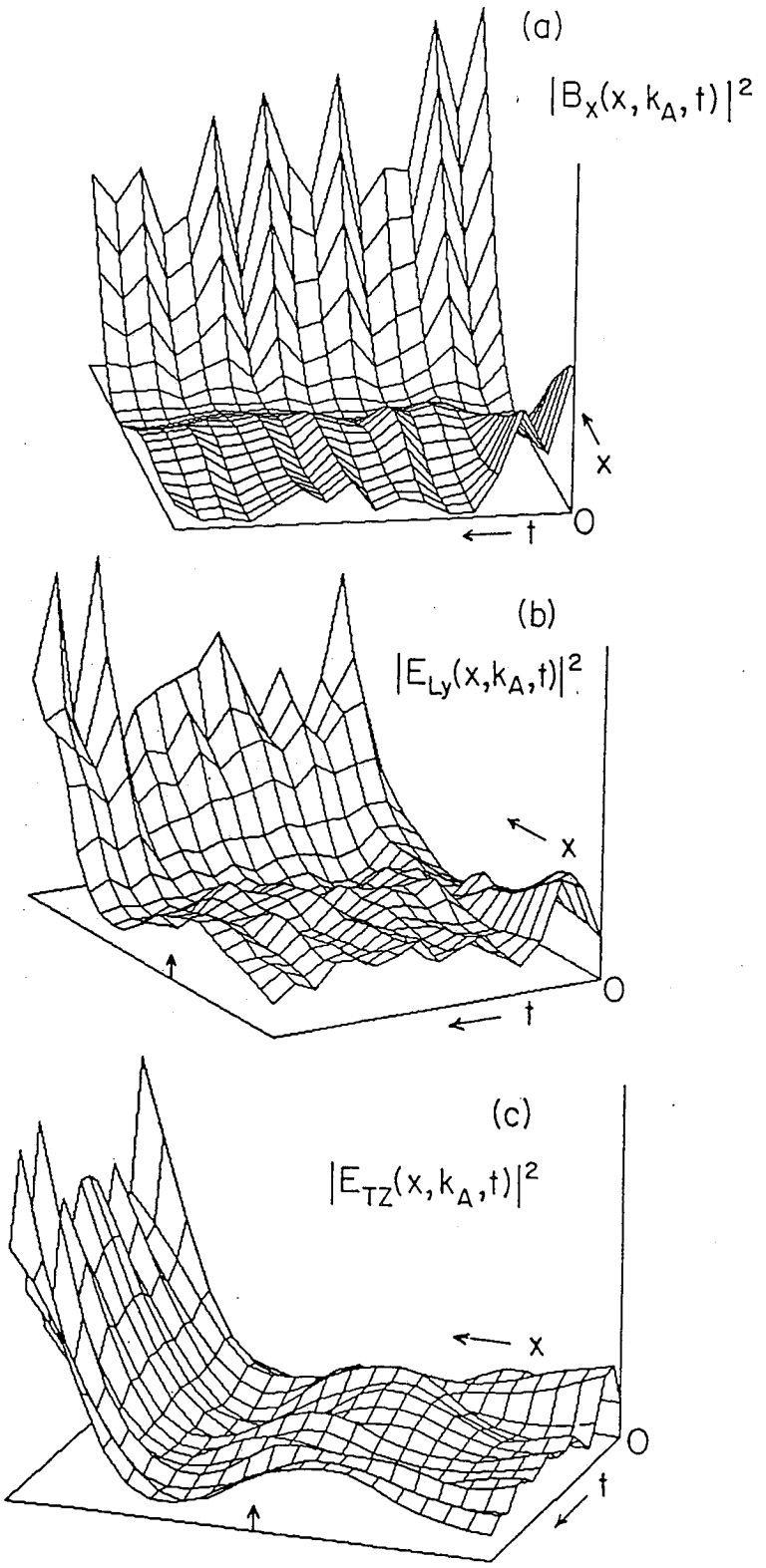

Fig. 18